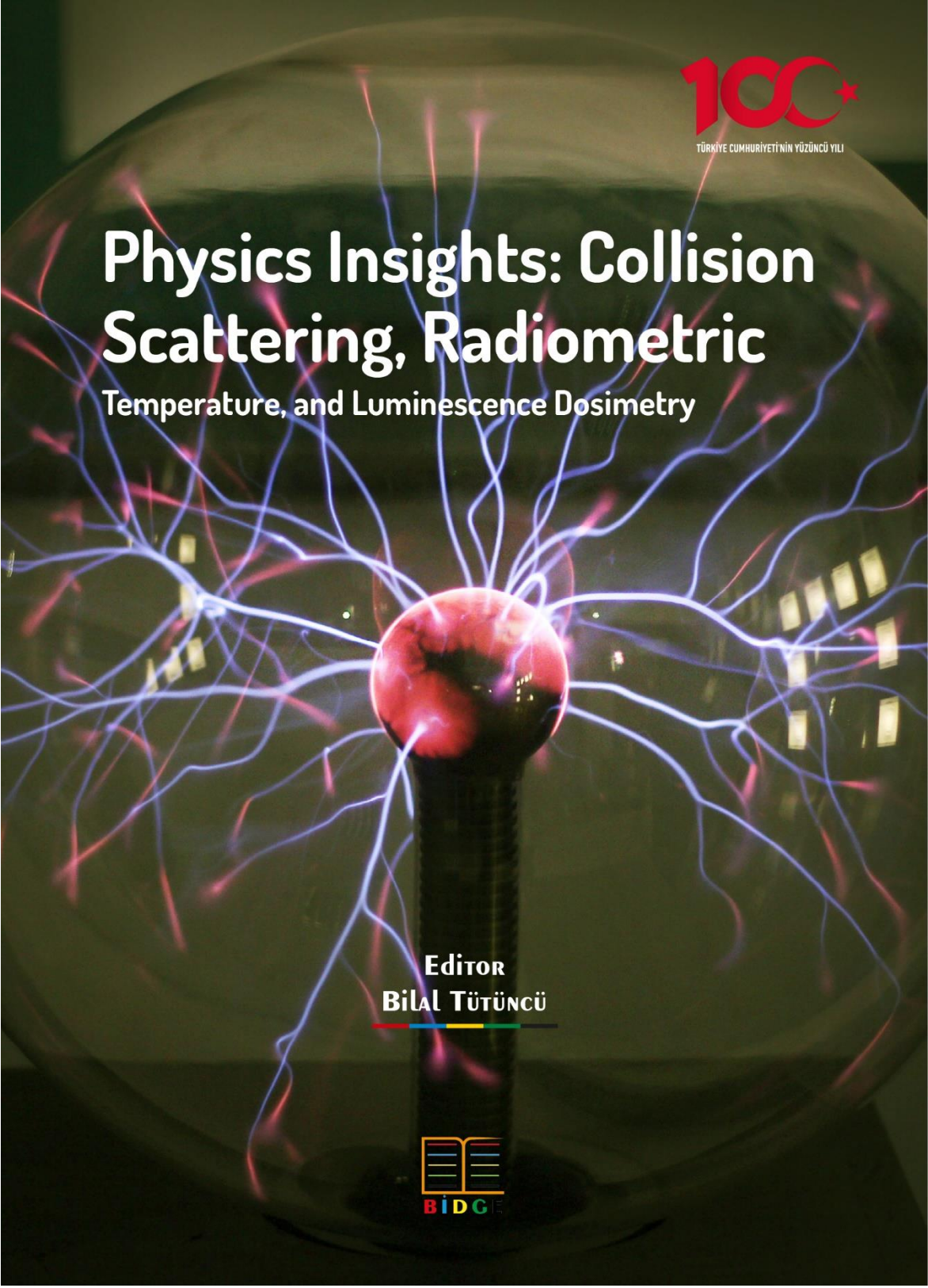
100
TÜRKİYE CUMHURİYETİ'NİN YÜZÜNCÜ YILI
Physics Insights: Collision Scattering, Radiometric
Temperature, and Luminescence Dosimetry
Editor
Bilal Tütüncü
BİDGE

BIDGE Publications

Physics Insights: Collision Scattering, Radiometric Temperature, and Luminescence Dosimetry

Editor: Doç. Dr. Bilal Tütüncü

ISBN: 978-625-372-202-9

Page Layout: Gözde YÜCEL

1st Edition:

Publication Date: 25.06.2024

BIDGE Publications,

All rights of this work are reserved. It cannot be reproduced in any way without the written permission of the publisher and editor, except for short excerpts to be made for promotion by citing the source..

Certificate No: 71374

Copyright © BIDGE Publications

www.bidgeyayinlari.com.tr - bidgeyayinlari@gmail.com

Krc Bilişim Ticaret ve Organizasyon Ltd. Şti.
Güzeltepe Mahallesi Abidin Daver Sokak Sefer Apartmanı No: 7/9 Çankaya / Ankara

PREFACE

This collection, "Physics Insights: Collision Scattering, Radiometric Temperature, and Luminescence Dosimetry," serves as a comprehensive resource for researchers, educators, and students engaged in the diverse and rapidly evolving fields of physics. The collected works in this book encompass pioneering studies and detailed analyses that reflect the latest advancements in understanding physical phenomena through innovative methodologies and theoretical approaches.

In the initial chapter, Elif Somuncu delves into the first two moments of classical isotropic and anisotropic induced collision scattering. This meticulous exploration of gas properties enhances our understanding of molecular interactions and provides valuable insights for applications ranging from gas detector development to medical gas detection.

Melda Patan Alper's chapter on radiometric temperature measurement addresses critical advancements in temperature measurement principles and the impact of emissivity on these measurements. Her work underscores the importance of accurate temperature measurement in scientific and industrial applications.

Engin Aslar's investigation into the minimum detectable dose (MDD) value in luminescence dosimetry presents a thorough application of TLD-100, TLD-600, and TLD-700 dosimeters. His research contributes significantly to the field of radiation dosimetry, offering new perspectives on dose measurement accuracy.

As the editor, I have had the privilege of overseeing the assembly of these exceptional contributions. I am deeply grateful to the authors for their dedication and to Gözde Yücel for her meticulous work on the page layout. Their combined efforts have ensured that this publication meets the highest standards of academic excellence.

It is my hope that this book will not only serve as an invaluable reference but also inspire further research and collaboration. The topics covered in this book are at the forefront of physics research, and I believe they will stimulate new ideas and discoveries that will drive the field forward.

Editor

Doç. Dr. Bilal Tütüncü

Content

PREFACE 3

The first two moments of classical isotropic and anisotropic induced collision scattering 6

Elif SOMUNCU 6

Advancements in Temperature Measurement: Principles of Radiometric Temperature Measurement and Emissivity's Impact on Temperature Measurements 22

Melda Patan Alper 22

Lüminesans Dozimetrelerde Minimum Dedekte Edilebilen (MDD) Doz Değerinin Belirlenmesi: TLD-100, TLD-600 Ve TLD-700 Dozimetreleri İçin Bir Uygulama 39

Engin AŞLAR 39

Numerical evaluation of second virial coefficient over Exp-6 potential 63

Elif SOMUNCU 63

Investigation of spectroscopic properties of Cu(II)-Acetazolamide/Nicotinamide complex by computational chemistry method: Molecular Modelling Study, ADME and Toxicology 86

Filiz ÖZTÜRK 86

Tuğba AYCAN 86

CHAPTER II

The first two moments of classical isotropic and anisotropic induced collision scattering

Elif SOMUNCU

Introduction

Determining the physical and chemical properties of gases has a critical role in scientific and technological research. These properties need to be determined in several important application areas, such as the development of gas detectors, the characterization of refrigerants used in refrigerators and air conditioning systems, applications in fuel production processes, and the detection of gases used in medicine. These application areas can of course be expanded further. Therefore, both theoretical and experimental methods are recommended for detailed investigation of the physical and chemical properties of gases (Hirschfelder et al., 1954; Prausnitz et al., 1999; Mamedov et al., 2014; Mamedov et al., 2018; Somuncu et al. al., 2020). The Van der Waals and Peng-Robinson equations of state can be given as examples to theoretical methods. However, every equation of state has boundary conditions. Therefore, to describe the thermodynamic properties of gases more precisely, an equation of

state is needed that allows theoretical calculations to be made in wide ranges such as temperature and pressure. In this context, the virial equation of state comes to the fore. This equation of state allows the calculation of temperature-dependent thermodynamic properties by considering the interaction potentials between atoms and molecules. The virial equation of state is used to calculate the temperature-dependent thermodynamic properties of gases by considering the interaction potentials between atoms and molecules. This equation allows the determination of transport properties of gases such as enthalpy, free energy, Gibbs energy, thermodynamics and diffusion coefficient, viscosity, and thermal conductivity. (Hirschfelder et al., 1954; McQuaarie et al., 1997; O'connell et al., 2005; Kaplan 2006).

$$\frac{P}{k_B T} = \rho + B_2(T)\rho^2 + B_3(T)\rho^3 + B_4(T)\rho^4 + \cdots$$

Eq. (1) shows the viral equation of state. Here P is the pressure, k_B is the Boltzmann constant, T is the temperature and ρ is the density. $B_2(T)$, $B_3(T)$ and $B_4(T)$ are the second virial, third virial and fourth virial coefficients, respectively. The second virial coefficient is defined following form:

$$B_2(T) = -2\pi N_A \int_0^\infty (e^{-u(r_{12})/k_B T)} - 1) r_{12}^2 dr_{12}$$

Here $u(r_{12})$ is the intermolecular interaction potential. Examples of atomic and intermolecular interaction potentials can be given as Lennard-Jones, Exp-6, Kihara, MMSV and Yukawa potentials

(Kaplan, 2006). These potentials are determined according to the structures of atoms or molecules. Many physical and chemical properties of gases can be examined with these potentials. Moment calculations of induced collision scattering of gases can be made by using the interaction potentials between atoms and molecules in addition to such calculable properties. (Zarkova et al., 1995; 2002; Zarkova et al., 2002; El-Kader and Yulia, 2016). One of these features is the first two moments of induced collision scattering (Barocchi et al., 1976; El-Kader et al., 2017; Oh, 2008; El-Kader and Yulia, 2016).

First two moments of classical isotropic and anisotropic induced collision scattering

Collision-based spectroscopies reveal fundamental information about phenomena caused by intermolecular interactions. Colliding pairs of molecules in the condensed phase show an absorption band in the far-infrared region of the spectrum. This absorption is due to the induced dipole moment resulting from the distortion of electronic clouds during the collision of two molecules. Since the induced dipole moment depends on the distance between the colliding pair, the translational state of the system may change due to the interaction of the induced dipole with the electromagnetic field, leading to a rotational absorption band. Measurements of collision-induced absorption (CIA) spectra therefore provide information about interatomic interactions. Specifically, the spectral line shapes and intensities reflect specific details of the induced dipole as a function of interatomic separation and collision dynamics (i.e., interatomic potential). Another level is the collisions of liquids and dense gases in isotropic and anisotropic induced light scattering that occur due to collisional interactions. Here, two functions of interatomic

separation, interatomic interaction potentials, and induced polarizability have strong spectra shaped by isotropic and anisotropic (El-Kader et al., 2015; El-Kader and Yulia, 2016; El-Kader et al., 2017).

Molecular interaction information can be obtained from these spectra. For the lower frequency portion of the spectra caused by this collision, the dipole-induced -dipole (DID) interaction explains most of the scattering intensities presented. But in the high frequency range (well region of the interatomic potential), electron exchange contributions must be considered and therefore the molecular pair against the dominant classical DID background is measurable. It is related to light scattering in isotropic and anisotropic induced collisions. These terms are determined in relation to the intermolecular interaction potential. The formula is obtained according to the potential parameters (Barocchi et al., 1976; Barocchain et al., 1977; El-Kader et al., 2017). The first two moments of isotropic and anisotropic induced collision scattering can be examined classically and quantumly. The first two moments of classical isotropic and anisotropically induced collisional scattering (Levine and Birnbaum, 1971).

Isotropic moments:

$$\phi_\alpha(0) = 4\pi \int_0^\infty [\alpha(r)]^2 e^{-u(r)/k_B T} r^2 dr$$

$$\phi_\alpha^2(0) = -4\pi \frac{k_B T}{m} \int_0^\infty \left(\frac{d\alpha(r)}{dr}\right)^2 e^{-u(r)/k_B T} r^2 dr$$

Anisotropic moments:

$$\phi_\beta(0) = 4\pi \int_0^\infty [\beta(r)]^2 e^{-u(r)/k_B T} r^2 dr$$

$$\phi_\beta^2(0) = -4\pi \frac{k_B T}{m} \int_0^\infty \left[\left(\frac{d\beta(r)}{dr} \right)^2 + 6 \left(\frac{\beta(r)}{r} \right)^2 \right] e^{-u(r)/k_B T} r^2 dr$$

It is defined as follows. Here β(r) is the double polarizability, β′(r) is the first order derivative with respect to r, u(r) is the atomic or intermolecular interaction potential, kB is the Boltzmann constant, T is the temperature and μ is the reduced mass. β(r) can be obtained from dipole-induced ,-dipole (DID) interactions. It is defined as isotropic or anisotropic depending on the structure of the atom or molecule (El-Kader and Yulia 2016). The low level DID equation for the isotropy and anisotropy that provides the interaction of two pairs of atoms is given by Eq.(7) (Levine and Birnbaum, 1971; Barocchi et al., 1976; El-Kader, 2015).

$$\alpha(r) = \frac{4\alpha_0^3 + \frac{5\gamma C_6}{9\alpha_0 r^6}}{r^6}, \quad \beta(r) = \frac{6\alpha_0^2}{r^3}$$

α_0 is the polarizability of the isolated atom and C_6 is the quadrupole polarization. Here, when the atoms get very close to each other, the electronic distribution overlaps and is expected to change a lot depending on r. This can be assumed especially in the case of absorptions in induced collisions of rare-gas mixtures. However, an

empirical approach has been proposed to represent all interaction effects that change faster than r_3. The DID at all levels for isotropy and anisotropy is given by Eq. (8) (El-Kader and Yulia, 2015).

$$\alpha(r) = \frac{4\alpha_0^3}{r^6 - \alpha_o r^3 - 2\alpha_0^2} + \frac{5\gamma C_6}{9\alpha_0 r^6}, \quad \beta(r = \frac{6\alpha_0^2 r^3}{r^6 - \alpha_o r^3 - 2\alpha_0^2})$$

Additionally, in the experimental model proposed by Bonechi and her colleagues, Eq. (10) is used to describe the polarization between two atoms.

$$\alpha(r) = f_6(r)\frac{A_6}{r^6} + B_1 \exp(\frac{-r}{r_{01}})$$

$$\beta(r) = f_3(r)\frac{6\alpha_0^2}{r^3} + f_6(r)\frac{A}{r^6} + B_2 \exp(\frac{r}{r_{02}})$$

The expressions in these equations are given as follows:

$$A_6 = 4\alpha_0^3 + \frac{5\gamma C_6}{9\alpha_0}, \quad A = 6\alpha_0^3 + \frac{\gamma C_6}{3\alpha_0}, \quad f_n(r) = 1 - e^{-br}\sum_{k=0}^{n}\frac{(br)^k}{k!}$$

Several scientists have described a three-parameter quasi-empirical model for DID based on classical mechanics (Meinander et al., 1985; Elliasmine et al., 1997).

$$\beta(r) = 6\alpha_0^2 r^{-3} + r^{-6}\left(6\alpha_0^3 + \frac{\gamma C_6}{3\alpha_0}\right) - B\exp(\frac{r}{r_0})$$

In Equation12, the first term is the first level for DID. The other terms are minor corrections in Equation 12. The second term is for medium-range effects and the exponential term is for short-range overlap effects. For pure spherical molecular gases in anisotropic light scattering cases, the DID is given by the equation (El-Kader et al., 2016).

$$\beta(r) = 6\alpha_0^2 r^{-3} + r^{-6}\left(6\alpha_0^3 + \frac{\gamma C_6}{3\alpha_0}\right) + \frac{24\alpha_0^2 C_6}{r^8} - B\exp(\frac{r}{r_0})$$

In Eq. (13), the third term has been added differently. Here the first two terms are the first and second level DID contributions. The last terms represent electronic overloping effects on polarization. In addition, in the case of pure xenon, the DID equation for the double polarization resulting from light scattering in induced collisions is given by.

$$\beta(r) = 6\alpha_0^2 r^{-3} + r^{-6}\left(6\alpha_0^3 + \frac{\gamma C_6}{3\alpha_0}\right) - (D = 25806\alpha_0^2 r_m^3)\exp(-\frac{r}{0.09531 r_m})$$

As can be seen from the equations proposed for isotropic and anisotropic DID, new terms have been added to better examine the physical structure of the atom or molecule.

There are many examples of both numerical and experimental studies in the literature regarding light scattering due to induced collisions in gases (Barocchi et al., 1976; Barocchaın et al., 1977; Zarkova et al., 1995; 2002; Zarkova et al., 2002; El-Kader, 2016). A detailed examination of the collision spectrum of induced light scattering provides interesting information about molecular motion in a dense medium. This examination can be used to check molecular interaction potential patterns as well as induced polarizability patterns. To date, several papers on moment analysis of the collision spectrum of induced light scattering have examined possible models of the induced polarizability pattern, with an emphasis on the Lennard-Jones interaction potential. (Barocchi et al., 1976; Somuncu et al., 2021). However, we observe that very little work has been done in the literature for other interaction potentials. However, there are many interaction potentials that enable sensitive and accurate examination of the physical and chemical properties of many atoms or molecules, which better define their structure. It is seen that some studies in this field have been analyzed numerically. However, it is known that numerical calculations are insufficient due to boundary conditions. For this reason, analytical studies need to be carried out, and analytical studies on this subject are quite limited. To overcome this deficiency, it is aimed to obtain analytical expressions by considering different molecular interaction potentials in the first two moment equations of the collision spectrum of induced light scattering (Barocchi et al., 1976; Zarkova et al., 2002; El -Kader, 2016; Somuncu et al., 2021).

Selection of atomic and intermolecular interaction potentials is very important to calculate the first two moments of induced collision scattering of gases (Barocchi et al., 1977; Meinander et al., 1986; El-Sheikh et al., 1989; Tabisz et al., 1995; Kaplan 2006). Interaction potentials between atoms and molecules must be determined in a way that defines the properties of gases. In addition, appropriate parameters must be determined for the atomic and intermolecular interaction potential parameters of the selected gases so that the moment calculations can be sensitive and accurate. For this reason, the parameters must be determined accurately and precisely to calculate the physical and chemical properties of the examined gas using atomic and intermolecular interaction potentials. Depending on the chosen atomic and intermolecular interaction potentials, the calculation of the first two moments of induced collision scattering generally involves great difficulties, so analytical formulas have not yet been derived. In the existing literature, it is seen that such calculations are largely carried out with numerical methods (Barocchi et al., 1976; Barocchaın et al., 1977; Zarkova et al., 1995; Kirch et al., 2002; Zarkova et al., 2002; Oh, 2008; El-Kader, 2016; El-Kader et al., 2017). It is well known that numerical calculation methods provide accurate results within a limited range of parameters, but the calculations are time-consuming and unsuitable for many systems. Therefore, researchers have developed various numerical approaches to overcome these limitations. However, it is known that these integral calculations cannot be solved exactly due to some limitations. Numerical methods are convenient to work within certain parameter limits but are generally not applicable for different parameter sets. Therefore, while numerical calculation methods can produce accurate results for a limited range of

parameters, they do not provide complete solutions. Additionally, numerical methods do not provide exact solutions. In this context, the lack of analytical methods on how moments can be calculated over different interaction potentials stands out. In cases where many different atomic or molecular interaction potentials are used, analytical calculation of the moments of gases emerges as one of the most important physical problems of today. Therefore, many theoretical and experimental works are suggested for evaluating of the moment of the CIS in literature (Barocchi and Zoppli,1976; McTague and Birnbaum,1971). The choice of reliable molecular pair potentials is important for accurate and precision calculations of moments of CIS. Note that, in the literature, the theoretical method (Barocchi and Zoppli,1976) has been presented for the determination of the moment of CIS with Lennard-Jones (12-6) potential. But Lennard-Jones (2n-n) potential can be not used for calculating of moments of CIS of gases. Therefore, a new analytical formula for the calculation of the first two moment of CIS with Lennard-Jones (2n-n) is presented firstly, which considerably developed its ability throughout analytical evaluations of significant cases by Somuncu and Gökbulut. Therefore, the suggested analytical expression for the moment of CIS with Lennard-Jones (2n-n) potential has the main importance.

Definition and Expressions for the first two moments of CIS

The first two moments of the two body CIS are defined following as (Levine and Birnbaum, 1971; Levine, 1972):

$$\varphi^{(0)} = 4\pi \int_0^\infty \beta_{12}^2 g_0\left(r_{12}\right) r_{12}^2 dr_{12} \qquad (15)$$

$$\varphi^{(2)} = -4\pi \frac{k_B T}{m} \int_0^\infty \left(\left(\frac{d\beta_{12}}{dr_{12}} \right)^2 + 6 \left(\frac{d\beta_{12}}{dr_{12}} \right)^2 \right) g_0(r_{12}) r_{12}^2 dr_{12} \qquad (16)$$

where $\varphi^{(0)}$ and $\varphi^{(2)}$ anisotropic moments, k_B is Boltzmann constant, T is temperature and m is reduced mass. β_{12} is induced polarizability and the classical dipole-induced-dipole (DID) approach is expressed as

$$\beta_{DID}(r_{12}) = \frac{6\alpha^2}{r_{12}^3} \qquad (17)$$

Here, α is polarizability of the isolated atom (Gharbi and Duff, 1077). Substitute Eq. (17) into Eqs. (15)- (16) are obtained the formulae:

$$\varphi^{(0)} = \frac{144\pi\alpha^4}{b^3} I_4(T^*), \ldots\ldots\ldots\ldots\ldots\ldots\ldots\ldots\ldots\ldots\ldots\ldots\ldots\ldots...(18)$$

$$\varphi^{(2)} = -144\pi \frac{k_B T \alpha^4}{m\, b^5} I_6(T^*), \ldots\ldots\ldots\ldots\ldots\ldots\ldots\ldots\ldots\ldots\ldots\ldots(19)$$

where b is normalization length , $T^* = k_B T/\varepsilon$ is reduced temperature and $x = r_{12}/b$

$$I_k(T^*) = \int_0^\infty x^{-k} e^{-u(x)/T^*} dx \qquad (20)$$

where $u(x)$ intermolecular interaction potential. The potential considered in Eq.(20) is the Lennard-Jones (2n-n) potential.

$$u(r) = 4\varepsilon \left(\left(\frac{\sigma}{r} \right)^{2n} - \left(\frac{\sigma}{r} \right)^{n} \right).$$

Here, ε is the depth of potential well, σ is the value r at $u(r)=0$ (Kaplan, 2006)

Substitute Lennard-Jones (2n-n) potential into Eq. (6), we obtain the following formula:

$$I_k\left(T^*\right)=\int_0^\infty x^{-k}e^{-\frac{4}{T^*}\left(x^{-2n}-x^{-n}\right)}dx \tag{21}$$

By solving the integral, we obtain the analytical formula (Somuncu and Gökbulut):

$$I_k\left(T^*\right)=\frac{1}{n}\left(\frac{8}{T^*}\right)^{-\left(\frac{k-1}{2n}\right)}e^{\frac{1}{2T^*}}\Gamma\left(\frac{k-1}{n}\right)D_{(1-k/n)}\left(-\sqrt{2/T^*}\right) \tag{22}$$

where $\Gamma(\alpha)$ is the gamma function and $D_v(z)$ is the parabolic cylinder function. Substitute Eq. (22) into Eqs. (15)-(16), we obtain analytical formulae for first two moments of CIS.

Table 1. Comparative calculation results of moment $\varphi^{(0)}\left(A^9\right)$

		Lennar-Jones (12-6) for Argon			Lennar-Jones (12-6) for Krypton		
$T(K)$	k	This work	Mathematica numeric results	Experimental (Barocchi, et al, 1976)	This work	Mathematica numeric results	Experimental (Barocchi, et al, 1976)
50	4	137.507	137.507	-	1380.88	1380.88	-
100		59.3513	59.3513	-	368.972	368.972	-
200		42.6509	42.6509	-	215.042	215.042	-
300		39.4692	39.4692	30.2	186.589	186.589	93.5
400		38.536	38.536	–	176.496	176.496	–
500		38.327	38.327	–	172.215	172.215	–
600		38.4199	38.4199	–	170.417	170.417	–
700		38.6562	38.6562	–	169.863	169.863	–
800		38.9651	38.9651	–	169.995	169.995	–
900		39.3112	39.3112	–	170.532	170.532	–
1000		39.6756	39.6756	–	171.315	171.315	–

As seen from Table 1, the analytical formula is conceptually valid in various temperature ranges, and it offers many advantages over other methods. The analytical formula is entirely general and free of any limitation on its implementations.

References

Barocchi, F. & Zoppi, M. (1976) Determination of collision induced polarizability in Ar, Kr, and Xe by means of collision induced scattering analysis and empirical pair potentials. *The Journal of Chemical Physics,* 65.3, 901-905. Doi: 10.1063/1.433157.

Barocchi, F., et al. (1076) A comparison of the spectral features of the collision-induced light scattering by the molecular gases CH_4 and CF_4 and by argon. *Canadian Journal of Physics,* 55.22, 1962-1969. Doi: 10.1139/p77-239

El-Kader, M. S. A. & Yulia N. K. (2016) Dipole–octupole polarisability of uranium hexafluoride and theoretical prediction of anisotropic light-scattering spectrum using new intermolecular potential. *Molecular Physics,* 114.1, 44-52. Doi: 10.1080/00268976.2015.1082653

El-Kader, M. S. A., et al. (2017) Spectral line shapes of collision-induced light scattering (CILS) and collision-induced absorption (CIA) using isotropic intermolecular potential for H2–Ar. *Molecular Physics* 115.20, 2614-2625. Doi: 10.1080/00268976.2017.

El Kader, M. S. A. (2015) Collision-induced light scattering spectra of mercury vapour at different temperatures. *Molecular Physics,* 113.11, 1368-1377. Doi: 10.1080/00268976.2014.994569

Elliasmine, A., J-L. Godet, & Yves Le Duff. Depolarized light scattering by CF_4. *Molecular Physics* 90.2 (1997): 147-157.

El-Sheikh, S. M. & Tabisz, G. C. (1989) Perturber dependence of the collision-induced light scattering by SF6 and CF4. *Molecular Physics: An International Journal at the Interface Between*

Chemistry and Physics. 68, (6) 1225-1238. Doi: 10.1080/00268978900102861

Gharbi, A., Le Duff, Y., Physica 87A (1977) 177.

Hirschfelder, J. O., Curtiss, C. F. & Bird, R. B. (1954). *Molecular Theory of Gases and Liquids*. New York: Jonh Wiley &Sons.

Kaplan, I. G. (2006). *Intermolecular Interactions: Physical Picture. Computational Methods and Model Potentials*. New York: Jonh Wiley & Sons.

Kirch, P. & Rolf S. (1965). Measurement of thermal diffusion and determination of the intermolecular potential of gaseous uranium hexafluoride. *The Journal of Chemical Physics* 42.10, 3729-3730.

Levine, H. B. (1972) Spectroscopy of Dimers. *Journal of Chemical Physics* 56, 2455. Doi: 10.1063/1.1677554

Levine, H. B. & Birnbaum G. (1971) Determination of Models for Collision-Induced Polarizability by the Method of Moments. *The Journal of Chemical Physics* 55.6, 2914-2917. Doi: 10.1063/1.1676514

Mamedov, B. A. & Somuncu E. (2014) Analytical treatment of second virial coefficient over Lennard-Jones (2n− n) potential and its application to molecular systems. *Journal of Molecular Structure* 1068, 164-169. Doi: 10.1016/j.molstruc.2014.04.006

Mamedov, B. A., Somuncu E. & Askerov, I. M. (2018) Evaluation of speed of sound and specific heat capacities of real gases. *Journal of Thermophysics and Heat Transfer* 32.4, 984-998. Doi:10.2514/1.T5285

McQuarrine, D. A. & Simon, J. D., (1997). *Physical Chemistry: A Molecular Approach*. USA: University Science Book.

McTague, J. P. & Birnbaum, G. (1971) Collsion-induced light scarttering in gases I. the gases:Ar, Kr, and Xe. *Physical Review A* 3, 1376. Doi: 10.1103/PhysRevA.3.1376

Meinander, N., Tabisz, G. C., Zoppi, M. (1986) Moment analysis in depolarized light scattering: Determination of a single parameter empirical pair polarizability anisotropy for Ne, Ar, Kr, Xe, and CH4. *The Journal of Chemical Physics* 84, 3005. Doi: 10.1063/1.450281

Prausnitz, J. M., Lichtenthaler, R. N. & Azevedo, E. G. de (1999). *Fugacities in Gas Mixtures. Molecular Thermodynamics of Fluid-Phase Equilibria*. New Jersey: Prentice- Hall.

Somuncu, E., Emek, M. & Mamedov, B. A. (2020) Unified Analytical Formulae of Second Virial Coefficient with Kihara Potential and its Application to Real Gases. *Acta Physica Polonica* 137 (3), 293-299. Doi: 10.12693/APhysPolA.137.293

Somuncu, E. & Gokbulut, M. (2021) Analytical evaluation of moments of collision-induced scattering with Lennard-Jones (2n-n) potential. *Zeitschrift für Physikalische Chemie* 235.6, 805-813. Doi: 10.1515/zpch-2019-1535

O'connell J. P. & Haile J. M. (2005). *Thermodynamics Fundamentals of Applications*, New York, Cambridge University Press.

Oh, S. K. (2008) Application of the group contribution concept to Kihara potential for estimating thermodynamic and transport properties: Part VI. Heavy globular molecules (SF_6, MoF_6, WF_6,

UF_6, $C(CH_3)_4$, $Si(CH_3)4$). *Fluid phase equilibria* 271.1-2, 53-68. Doi: 10.1016/j.fluid.2008.07.005

Tabisz, G.C. & Neuman, M. N., (1995). *Collision- and Interaction-Induced Spectroscopy. Nato ASI Series*, Springer-Science+Business Media.

Zarkova, L., & Pirgov, P. (1995) Transport and equilibrium properties of UF_6 gas simultaneously fitted by an effective isotropic potential with temperature-dependent parameters. *Journal of Physics B: Atomic, Molecular and Optical Physics* 28.19, 4269. Doi: 10.1088/0953-4075/28/19/012

Zarkova, L., & Hohm, U. (2002) pVT–Second Virial Coefficients B (T), Viscosity η (T), and Self-Diffusion ρD (T) of the Gases: BF_3, CF_4, SiF_4, CCl_4, SiCl4, SF_6, MoF_6, WF_6, UF_6, $C(CH_3)_4$, and $Si(CH_3)_4$ Determined by Means of an Isotropic Temperature-Dependent Potential. *Journal of Physical and Chemical Reference Data* 31.1, 183-216. Doi: 10.1063/1.1433462

CHAPTER II

Advancements in Temperature Measurement: Principles of Radiometric Temperature Measurement and Emissivity's Impact on Temperature Measurements

Melda Patan Alper

Introduction

Temperature, a fundamental property of matter, has been measured and studied for centuries. Throughout history, various methods have been developed to measure temperature, from simple observations of changes in the state of matter to the use of standardized temperature scales such as Kelvin, Celsius, and Fahrenheit. These early methods laid the foundation for the scientific understanding and measurement of temperature, enabling advances in fields such as basic science, engineering and meteorology [1,2]. In 2019, a significant revision occurred in the definition of the SI unit of temperature, the kelvin, one of the 7 fundamental units, making it compatible with the Boltzmann constant and increasing its precision and universality [3]. This revision marked a historical moment in

temperature measurement; It reflected ongoing efforts to refine and standardize scientific units for greater accuracy and consistency across disciplines.

In recent years, we have witnessed remarkable advances in temperature sensing technologies, driven by rapid developments in some fields (for example: materials science, electronics, medicine and nanotechnology). These advances have led to the emergence of particularly complex devices such as radiation thermometers, which have revolutionized precise temperature measurements. Radiation thermometers, also known as infrared thermometers or pyrometers, are a NASA technology and work on the principle of detecting the infrared radiation emitted by an object to determine its temperature. Unlike traditional types of contact thermometers, radiation thermometers offer non-invasive temperature measurement solutions, making them ideal for applications where physical contact is impractical or undesirable [4,5]. Their most cited features, fast response times, wide temperature measurement range, and ability to measure remote or inaccessible objects, make them indispensable tools in a variety of industries, including manufacturing, transportation, aerospace, medical, and food processing.

Advances in temperature measurement have expanded to include calibration techniques and sensor technologies, and the accuracy and precision of measurements have become even more important. As we know, calibration plays a very important role in ensuring the accuracy and reliability of temperature measurements. The calibration method in temperature measurements is based on comparing the measurement result of a temperature sensor or device to be tested with a known reference standard to identify any

deviations or errors. Calibration laboratories use precision techniques and equipment to calibrate temperature sensors according to the ISO/IEC 17025 standard and traceable devices to international standards, thus ensuring consistency and accuracy of temperature measurements across different devices and laboratories. Sensor technologies have also advanced significantly with the development of highly sensitive and accurate thermometer sensors based on various operating principles, such as different types of thermometers, such as resistance sensors (RTDs), thermocouples, and semiconductor sensors (6). These sensors contribute to advances in temperature measurement and monitoring capabilities, finding applications in a wide variety of fields, from environmental monitoring and industrial process control to medical diagnostics and consumer electronics.

In this study, we aim to provide a comprehensive overview of radiation thermometers, which have been used quite frequently in the last 20 years, by discussing their operating principle, applications and methods for estimating measurement uncertainty. However, by exploring the importance of calibration and advances in temperature sensor technologies in ensuring accurate and precise temperature measurements, we aim to equip readers with a comprehensive perspective on temperature measurement principles, applications and technologies in modern applications.

Basic Principles of Radiometric Temperature Measurement

The principle of radiometric temperature measurements is based on measurements of the thermal radiation emitted by objects to determine their temperature. Unlike measurements by traditional contact thermometers, radiometric temperature measurements do not

require physical contact with the object being measured; This makes them suitable for a wide variety of applications where contact methods are impractical or impossible.

Radiometric measurements are based on the laws of thermal radiation, specifically Planck's law, which describes the spectral distribution of thermal radiation emitted by an object at a given temperature (7). According to Planck's law (Equation 1), every object above absolute zero emits electromagnetic radiation, and the intensity and spectral distribution of this radiation is proportional to the temperature of the object.

B spectral radiance of a body,

λ Wavelenght

T absolute temperature

k_B Boltzmann constant

h Planck constant

c speed of light in the medium

$$B_\lambda(\lambda, T) = \frac{2hc^2}{\lambda^5} \frac{1}{e^{\frac{hc}{\lambda k_B T}} - 1} \qquad (1)$$

Radiometric thermometers, also known as radiation thermometers or pyrometers, detect and measure the thermal radiation emitted by an object to determine its temperature. Such thermometer sensors typically consist of an optical system, a detector and signal processing electronics. In the first part, the optical system collects the thermal radiation emitted by the object and focuses it on the detector. The detector converts the incoming radiation into an

electrical signal, which is then processed to calculate the temperature of the object.

Various factors affect the accuracy and reliability of measurements in radiometric temperature measurements. These include the emissivity value, which is the ratio of the radiation emitted by an object to the radiation emitted by a perfect blackbody at the same temperature and wavelength; ambient temperature and humidity, which may affect the thermal radiation emitted by the object and the performance of the sensor; and atmospheric conditions such as dust, smoke, or gases that may attenuate or scatter thermal radiation and affect measurement accuracy.

Radiometric temperature measurements find applications in a variety of industries and fields, including manufacturing, aerospace, automotive, agriculture and medical imaging. These measurements can be used for temperature monitoring and control in industrial processes, thermal imaging for predictive maintenance and troubleshooting, non-destructive testing of materials, and medical diagnostics, among others.

Understanding the basics of temperature measurement principles and techniques of this type is crucial to obtaining accurate and reliable temperature measurements in a variety of industrial and scientific environments.

Emissivity and Its Impact on Temperature Measurements

In radiometric temperature measurements, emissivity is the most critical factor affecting the accuracy and reliability of measurements. The emissivity value is defined as the ratio of the radiation emitted by an object to that emitted by a perfect blackbody at the same

temperature and wavelength. In summary, emissivity describes how efficiently an object emits thermal radiation relative to a blackbody (8,9).

This critically important emissivity value affects the amount of thermal radiation detected by the sensor. Objects with high emissivity emit radiation more effectively and appear "hotter" to the sensor, while objects with low emissivity emit less radiation and may appear cooler than their actual temperature. Therefore, accurate knowledge or determination of an object's emissivity value is crucial to obtaining precise temperature measurements.

Emissivity is not easy to determine accurately because it varies with factors such as surface roughness, composition and temperature. While some materials have relatively constant emissivity values over a wide range of wavelengths and temperatures, others exhibit significant differences. Additionally, surface conditions such as oxidation or contamination can alter an object's emissivity value, further complicating measurements.

A variety of techniques are used to detect emissivity, including spectrophotometry, thermal imaging, and empirical replicates. Spectrophotometric fluctuations include the report of reflectance and transmittance of materials at different wavelengths to obtain emissivity particles. Thermal imaging methods utilize replicated cameras to capture the thermal radiation emitted by the results and program the emissivity based on thermal signatures. Empirical measurements are resistant to calibration and reference for the quantification of particulate particles under controlled conditions (10).

The method frequently used for calibration laboratories, the most common method of determining the emissivity value of a material such as a blackbody, involves the features of a reference thermometer and a pyrometer with finely tuned emissivity settings. In this method, the reference thermometer is used for accurate use of actual temperatures, while the pyrometer divides the same temperature measurements. The emissivity value is then determined according to this compliance.

First, the reference thermometer is used to measure the temperature of the blackbody or the material whose emissivity is being determined. This reference thermometer provides an accurate measurement of the actual temperature.

Simultaneously, the pyrometer is aimed at the same blackbody or material. The pyrometer's emissivity setting is adjusted until it displays the same temperature reading as the reference thermometer.

Once the pyrometer's reading matches the temperature measured by the reference thermometer, the emissivity value used by the pyrometer at that setting is noted. This value represents the emissivity of the material at that particular temperature.

Importance of Calibration in Ensuring Accurate Temperature Measurements

According to the ISO/IEC 17025 standard in temperature metrology, it is very important to perform accurate and precise measurements of sensors and devices. Without proper calibration, temperature measurements may be inaccurate or different. This can lead to product quality reductions, manufacturing errors, and other problems. Therefore, frequent calibration of sensors and systems is

required to operate accurate and reliable measurements. Standardized calibration is created by accredited calibration laboratories and centers. Temperature sensors and devices are compared to a reference device over a period of time during calibration testing. Deviations from the reference device are corrected by electronic or mechanical modifications of the device. Temperature calibration is documented through calibration certificates. Calibration certificates contain the measurements obtained as a result of the calibration, the ranges within the recorded tolerance range, and the states in which the capacity is valid. Calibration certificates ensure that calibrated sensors or products can be operated at the manufacturer, in factories, laboratories or industrially. Proper calibration is necessary to obtain accurate temperature measurements in various industries. Many industries, from food processing to aerospace, rely on accurate temperature measurements to ensure product standards, standards and regulatory compliance. Therefore, to maintain measurement accuracy and performance, the installation must be integrated and performed by trained personnel. Calibration systems help maintain temperature sensors and devices, minimize measurement deviations and quality controls for various industries, improving product specifications and rates.

Calibration Method of Radiation Thermometers

The calibration of a radiation thermometer involves several steps to ensure accurate results. First, the emissivity value of the thermometer must be determined. This value reflects the ability of an object to emit and absorb thermal radiation, and it can vary depending on the type of material or surface the thermometer is

measuring. Once the emissivity value is known, temperature corrections are made to adjust the readings of the thermometer accordingly. To perform the calibration, a blackbody source is used as the reference standard. The blackbody source is a perfect emitter and absorber of thermal radiation and has a known temperature (11). The thermometer is placed at a specified distance from the blackbody source, and the focal length is tested before measurements. The calibration is carried out by comparing the calibration of the test thermometer to that of a reference standard. A reference resistance thermometer placed near the blackbody source is used as the reference standard. During calibration, the temperature of the blackbody source is measured with the reference resistance thermometer. The test thermometer is then calibrated by taking measurements at the same reference-test distance used for the reference resistance thermometer. The calibration is carried out at least in 5 points within the measurement range of the test thermometer. In addition to calibration at different temperatures, the size effect of the target (SET) is determined for each measurement point of the calibrated thermometer (12). The size effect of the target reflects the degree to which the size of the target influences the temperature measurement. It can be determined by scanning the target size of the thermometer, considering the diameter of the blackbody target. To ensure traceability, the blackbody target is calibrated separately, and the surface temperature distribution of the target is measured during calibration. This value is added to the measurement uncertainty budget to ensure accuracy in the calibration process.

Estimation of Measurement Uncertainty and Optimizing Uncertainty Budget

To prepare an uncertainty budget for radiation thermometers, the purpose and scope of the measurement should be identified first, including the temperature range and points to be measured. Uncertainty components such as emissivity, viewing angle, target surface characteristics, calibration-related uncertainties, and the time required for the thermometer to stabilize should be determined based on the measurement principles (13-17). The uncertainty values for each component can then be calculated using manufacturer specifications, calibration certificates, and other relevant documents. Type A uncertainty can be evaluated using statistical standard deviation from a series of repeated observations, while Type B uncertainty can be obtained from existing information such as uncertainties of equipment used, standards, and temperature and pressure changes. The total uncertainty is the square root of the sum of squares of A and B Type uncertainties, and the expanded uncertainty expresses the range of values that the measurement result may fall within with a certain level of confidence. The coverage factor (k=2 for %95 confidence level) may be used to account for the effects of uncertainty components related to each other (13). The uncertainty budget is crucial information that should be presented along with test or calibration results to ensure that the measurement results are reliable.

The following are the uncertainty parameters that affect the measurement of radiation thermometers:

Reference Thermometer Drift: The difference in mean values of the reference thermometer's last two years of certificates.

Reference Thermometer Certificate Uncertainty: The uncertainty value of the relevant temperature point in the last certificate of the reference thermometer.

Reference Thermometer Stability: The standard deviation of measurements taken with the reference at the temperature point during calibration.

Reference Display Uncertainty: The uncertainty value of the digital display on which the reference thermometer is connected.

Reference Display Drift: The average difference in measurement results from the last two years of measurements taken from the digital display on which the reference thermometer is connected.

Emissivity: The average difference in measurement results of a radiation thermometer calibrated at different emissivity values.

Blackbody Target Surface Temperature Distribution: The mean difference between the maximum and minimum values obtained from measurements taken at different areas of the blackbody target surface.

Source Stability: The standard deviation of measurements taken at the temperature point with the blackbody source for long-term stability.

IR Thermometer Stability: The standard deviation of 10 measurements taken at the calibrated temperature point of the radiation thermometer.

IR Thermometer Resolution: The number of significant digits that can be read from the radiation thermometer.

IR Thermometer Test Repeatability: The mean difference between the maximum and minimum values obtained from measurements taken at the calibrated temperature point with the radiation thermometer.

IR Thermometer Target Size Effect: The mean difference in measurement results obtained by changing the aperture size of the radiation thermometer.

Blackbody Emissivity: The value obtained from the emissivity correction and comes from the black coating.

In temperature metrology, measurement uncertainty is as important as the accuracy and precision of measurement results. Some of the parameters affecting measurement uncertainty may arise from factors such as the effects of the reference standard, the stability of temperature sources, the effect of external radiation on measurement instruments, and the design of black bodies used in the measurement system.

In order to reduce uncertainty and increase the accuracy of temperature measurements, it is an effective way to choose liquid bath systems used as temperature sources among these parameters. Liquid baths reduce uncertainty caused by temperature changes by providing a stable and homogeneous temperature environment for the devices to be tested (18). Another source of uncertainty is the effect of external radiation on the black body used in the measurement system. Black bodies are used as references for temperature measurement, and any external radiation on the black body can cause a significant error in the measurement results. To reduce this uncertainty, black bodies can be designed to minimize

the effect of external radiation by eliminating areas exposed to radiation. In summary, reducing the uncertainty in temperature measurements can be achieved by balancing temperature sources using liquid baths and designing black bodies to minimize external radiation effects. These improvements; It contributes to more accurate and reliable temperature measurements, which are important in many fields, including scientific research, industrial processes and medical applications.

Conclusion

As a conclusion, temperature measurements are a field of science that requires precise and accurate measurements for many sectors (science, engineering, medicine and manufacturing). Over the years, various methods and techniques have been developed to measure temperature accurately and reliably. Recent advances in materials science, electronics and nanotechnology have led to the emergence of advanced devices such as radiation thermometers, which provide non-invasive fast and reliable temperature measurement solutions and have revolutionized temperature measurement capabilities.

Radiometric temperature measurements are based on the principles of thermal radiation emitted by objects to determine their temperature. Understanding the fundamentals of radiometric temperature measurement, including the laws of thermal radiation and factors that can affect measurement accuracy, is crucial to obtaining accurate and reliable temperature measurements in a variety of environments.

Emissivity value plays a crucial role in radiometric temperature measurements and significantly affects the accuracy and reliability

of temperature measurements. It can be difficult to measure the emissivity value accurately due to variations caused by factors such as the blackbody's surface roughness, material, and temperature. However, a variety of techniques are used to measure emissivity and obtain precise temperature measurements, including spectrophotometry, thermal imaging, and empirical methods.

Calibration is essential for temperature sensors to make accurate and reliable measurements. Without proper calibration, temperature measurements can be inaccurate or biased, leading to poor product quality, manufacturing defects, and other problems. Proper calibration methods involve comparing sensors and devices to a known reference standard to identify any deviations or errors and correcting them accordingly. Calibration procedures help ensure the performance and accuracy of temperature sensors and devices, minimize measurement biases, and improve quality control for various industries.

As a result, temperature measurement is vital for a variety of industries, and advances in temperature sensing technologies continue to improve measurement accuracy and reliability. Understanding the principles of radiometric temperature measurement, the impact of emissivity on measurements, the importance of calibration, and advances in temperature sensors are crucial to obtaining accurate and reliable temperature measurements in a variety of applications and environments.

References

Rusby R., 2013, The beginner's guide totemperature measurement, good practice guide no. 125, NPL

Coates P. and Lowe D., 2019, The Fundamentals of Radiation Thermometers (Boca Raton, FL: CRC Press)

Miguel A. Martin-Delgado, 2020, The new SI and the fundamental constants of nature, Eur. J. Phys. 41 063003

Lowe D., Battuello M., Machin, G., Girard, F., 2003, Temperature: Its Measurement and Control in Science and Industry, vol. 7, ed. by D.C. Ripple, B.C. Johnson, C.W. Meyer, R.D. Saunders, G.F. Strouse,W.L. Tew, B.K. Tsai, H.W. Yoon (AIP, Melville, New York), pp. 625–630

ASTM E644–11 Standard Test Methods for Testing Industrial Resistance Thermometer, 2011

Javaid M., Haleem A., Singh R.P., Rab S., Suman R., 2021, Significance of sensors for industry 4.0: Roles, capabilities, and applications, Sensors International, Volume 2, 100110

Ballico M., 2004, Radiation Thermometry, Monograph 12: NMI Technology Transfer Series First Edition, NPL

Ballico M., 2003, A Simple Experimental Technique For Estimation of the Band – pass of Infrared Radiation Thermometers, Temperature-Its measurement and control in Science and Industry, 607-612, American Institute of Physics.

Ballico M., 2000, A simple Technique for Measuring the Infrared Emissivityof Blackbody Radiators, 37, 295-300, Metrologia.

Monte C., Gutschwager B., Morozova S. P., Hollandt J.,2009, Radiation Thermometry and Emissivity Measurements Under Vacuum at the PTB, Volume 30, pages 203–219, International Journal of Thermophysics

Ring E. F. J., Hartmann J., Ammer K., Thomas R., Land D. and Hand J. W., 2010 Infrared and microwave medical thermometry Experimental Methods in Physical Sciences: Radiometric Temperature Measurements II Applications ed Z M Zhang, B K Tsai and G Machin (New York: Academic) vol 43 pp 394–458 ch 7

Pušnik, I.; Grgić, G.; and Drnovšek, J., System for the determination of the size-of-source effect of radiation thermometers with the direct reading of temperature, Measurement Science and Technology, 2006 IOP Publishing Ltd Volume 17, Number 6

EA Laboratory Committee 2013 EA-4/02 evaluation of the uncertainty of measurement in calibration

Yoon H, Saunders P, Machin G, Todd A D 2018, BIPM, Guide to the Realization of the ITS-90 Radiaiton Thermometry

ASTM E1256 – 11a Standard Test Methods for Radiation Thermometers (Single Waveband Type)

ASTM E2758 -15a Standard Guide for Selection and Use of Wideband, Low Temperature Infrared Thermometers

CCT-WG5 on Radiation Thermometry Uncertainty Budgets for Calibration of Radiation Thermometers below the Silver Point Version 1.71, Final Version, April 2008

Boles S., Pušnik I., Mac Lochlainn D., Fleming D., Naydenova I., Martin S., 2017, Development and characterisation of a bath-based

vertical blackbody cavity calibration source for the range −30 °C to 150 °C, Volume 106, , Pages 121-127, Measurement

CHAPTER III

Lüminesans Dozimetrelerde Minimum Dedekte Edilebilen (MDD) Doz Değerinin Belirlenmesi: TLD-100, TLD-600 Ve TLD-700 Dozimetreleri İçin Bir Uygulama

Engin AŞLAR[1]

Giriş

Lüminesans dozimetri, lüminesans özellik gösteren dedektörler aracılığı ile iyonlaştırıcı radyasyon dozunun ölçülmesine dayanmaktadır. Elde edilen lüminesans şiddeti materyal tarafından soğurulan radyasyon miktarı ile ilişkilidir (Yukihara & ark., 2022). Termolüminesans (TL) ve optik uyarmalı lüminesans (OSL) teknikleri, lüminesans dozimetride en yaygın kullanılan iki tekniktir (Chen & Pagonis, 2011). Bu teknikler sadece radyasyon dozimetrisi alanında değil aynı zamanda jeolojik ve arkeolojik materyallerin

[1] Dr., Ankara Üniversitesi, Nükleer Bilimler Enstitüsü, Medikal Fizik Bölümü, Ankara/Türkiye, Orcid: 0000-0002-1414-0317, easlar@ankara.edu.tr

tarihlendirilmesi gibi alanlarda da sıklıkla tercih edilmektedir (Aitken, 1985).

Lüminesans dozimetri alanı, personel dozimetri, çevresel dozimetri, klinik dozimetri ve yüksek doz dozimetrisi olmak üzere toplam dört bölümde incelenmektedir (McKeever & ark., 1995). Personel dozimetri alanında mesleki olarak maruz kalınan radyasyon dozları rutin olarak belirli periyotlar boyunca ölçülmektedir. Personel dozimetri alanı, kendi içerisinde extremite dozimetri, tüm vücut dozimetrisi ve cilt dozimetrisi olmak üzere üç kısımda incelenir. Extremite dozimetrisinde, doz ölçümü el, kol ve ayak gibi kısımların aldığı doz değerine odaklanırken, tüm vücut dozimetrisinde 1000mg.cm^{-2} derinlikte soğurulan (1 cm derinlik) doz eşdeğeri ile ilgilenilmektedir. Bu durumda etkin radyasyon tipleri gama ışınları, X ışınları (>15keV) ve nötronlardır. Cilt dozimetrisinde ise giriciliği daha düşük olan radyasyon tipleri (beta parçacıkları, <15keV'lik X ışınları) tarafından 5-10mgcm^{-2}'lik derinlikte (0.07cm derinlik) radyasyon doz eşdeğeri ölçümleri yapılmaktadır. Çevresel dozimetri alanında ise özellikle insan yapımı radyasyon kaynaklı etkinliklerden kaynaklanan (nükleer santraller, yakıt transferleri ve dönüşümleri vb.) durumlarda çevrenin aldığı radyasyon doz değeri araştırılmaktadır. Çevresel dozimetride temel radyasyon kaynağı genelde gama yayınlayıcılar olarak kabul edilir. Kozmik radyasyon kaynaklı uzay dozimetrisi de çevresel dozimetri kapsamına girmektedir. Klinik radyasyon dozimetrisi alanında ise radyoterapi ya da diagnostik radyoloji gibi hem tedavi hem de teşhis aşamalarında radyasyon dozları ölçülmektedir. Son uygulama alanı olan yüksek doz dozimetrisinde ise nükleer reaktörlerin içi, materyal testleri ve yiyecek

sterilizasyonu gibi yüksek dozların bulunduğu alanlardaki radyasyon doz ölçümlerini kapsamaktadır. Bu alanda kullanılacak dozimetrelerin maruz kaldığı yüksek doz aralığı (>100Gy) sebebiyle kristallerin olası radyasyon hasarına karşı dikkatli olunmalıdır (McKeever & ark., 1995).

Ticari adıyla TLD-100 olarak bilinen LiF kristallerine Mg ve Ti elementlerinin katkılandırılması sonucu LiF:Mg,Ti dozimetreleri üretilmiştir. LiF materyalinin TL dozimetresi olarak ilk kullanımı 1950 yılların başında gerçekleştirilmiştir (Daniels & ark., 1949). Ardından Cameron ve arkadaşları tarafından 1963 yılında TLD-100 olarak patenti alınmıştır (Cameron & ark.,1963). Dozimetrelerin küçük boyutları, yüksek lüminesans hassasiyetine sahip olmaları, tekrarlanabilirliğinin iyi olması, toksik olmaması, kararlı piklerinde düşük sönüme uğraması ve ışıktan etkilenmemeleri gibi özellikleri sayesinde TLD-100 dozimetreleri medikal alanda radyasyon dozlarının ölçülmesinde çok yaygın bir şekilde kullanılmaktadır (Kron, 1994). Buna ilaveten TLD-100 dozimetrelerinin etkin atom numarasının dokunun etkin atom numarasına yakın olması sayesinde dozimetrelerin düşük enerji bölgesinde (<100keV) enerji bağımlılığının düşük olmasını sağlamaktadır (Bos, 2001). Bu sayede özellikle mamografi gibi düşük X ışını enerjilerinde dozimetreler güvenle kullanılabilmektir (Ekinci & Aşlar, 2024). Ayrıca iyon odaları ya da MOSFET tipi dozimetreler gibi herhangi bir kabloya ihtiyaç duyulmaması sayesinde kristal tipli dozimetreler canlı içi (*in vivo)* ölçümlerde yaygın bir şekilde tercih edilmektedir (Aznar, 2008).

TLD-100 dozimetreleri ışıma eğrisinde iç içe geçmiş temel olarak 6 tane pikten oluştuğu kabul edilmektedir (McKeever & ark.,

1995). Bunlardan 1. ve 2. pikler kararsız pikler olarak kabul edilirken, 5. pik dozimetrik pik olarak kabul edilmektedir (Bos, 2006). Bu pikler belirli yarı ömürlere sahiptirler. Radyasyon doz hesabında kararsız pikler kısa sürede sönüme uğradıkları için genellikle ön ısıtma işlemine tabi tutularak bu pikler kaybolduktan sonra geriye kalan pikler aracılığı ile doz değerlendirme işlemi yapılır. Dozimetrelerin tekrar tekrar kullanılabilmeleri için dozimetrelerdeki daha önceki kullanımlara ve doğal radyasyon dozuna karşı tuzaklardaki yüklerin tamamen boşaltılması amacıyla dozimetreler tavlama işlemine tabi tutulmaktadır. TLD-100 için standart tavlama işlemi 400ºC'de 1 saat ve bunu takiben 100ºC'de 2 saat olarak uygulanmaktadır. Ön ısıtma işlemi ise 100ºC'de 10 dakika olarak uygulanmaktadır (Furetta, 2010).

LiF ailesinden diğer dozimetre türleri ise bu bileşiğe farklı lityum izotoplarının katkılandırılması ile oluşturulan TLD-600 ve TLD-700 dozimetreleridir. TLD-600 dozimetrelerinde ana bileşikteki lityum elementinin ^{6}Li ve TLD-700 de ^{7}Li element yüzdeleri farklıdır. Lityum elementinin farklı izotoplarının nötronla etkileşim tesir kesitleri farklı olduğundan TLD-600 ve TLD-700 dozimetreleri nötron radyasyonun dedeksiyonunda tercih edilmektedir (McKeever, 1985).

Lüminesans dozimetrelerde minimum dedekte edilebilen doz (MDD) değerinin araştırılması hem TL hem de OSL teknikleri için dozimetrelerin ölçüm performansını anlama açısından önemli bir niceliktir. Karşılaştırmalı olarak belirlenen MDD değeri ilgili alanda kullanılacak dozimetrelerle ile ilgili minimum ölçülebilecek doz değeri hakkında genel bilgi sağlamaktadır. MDD değeri Eşitlik (1) aracılığı ile belirlenmektedir (Hirning, 1992):

$$MDD = 3\sigma\,\phi \quad (1)$$

Burada σ, fırın sonrası dozimetreler üzerinde hiçbir doz yokken doğal fon sayım (background) değerlerinden elde edilen lüminesans şiddet değerlerinin standart sapmasını, 3σ ise MDD'nin belirlenmesinde %99.7 güven aralığında olmasını, son olarak ϕ değeri ise sayım değerinden doza geçiş için gerekli kalibrasyon faktörünü göstermektedir.

MDD değeri, genel olarak kristal tipi, kristalin lüminesans hassasiyeti, ölçüm geometrisi ve cihaz dedeksiyon sistemi gibi birçok parametreye bağlıdır (Harvey, 2011; Rawat & ark., 2014). Aynı radyasyon kaynağı altında aynı doza maruz bırakılan benzer kütledeki iki farklı dozimetre türünden elde edilen lüminesans şiddet değeri yüksek olan dozimetre için MDD değeri daha düşük olacaktır. Dolayısıyla bu dozimetre türü ile daha düşük doz değerlerinin ölçülebilmesi mümkün hale gelecektir. Bununla birlikte hem dedeksiyon sistemlerindeki iyileştirmeler hem de deneysel metotlar ile geliştirilecek ölçüm protokolleri sayesinde MDD değerinin düşürülebilmesi mümkün hale gelebilmektedir (Burke & Sutton, 1997; Sadek, 2020).

Horowitz & Moscowith (1986), TLD-100 için MDD değerini hem standart analiz ile hemde piklerine ayrıştırma yöntemi ile araştırmışlardır. Bunun sonucunda MDD değerini yüzde 20 belirsizlikle standart analiz ile 27μGy, piklerine ayrıştırma yöntemi ile 1.9μGy elde etmişlerdir. Horowitz & ark. (2007) tarafından yapılan diğer bir çalışmada yüksek sıcaklık pikleri (pik 6 ve 7) ile ilişkili piklerin dahil edilmediği durumda TLD-100 dozimetreleri için MDD değerinin 3μGy'e kadar ölçülebileceği gösterilmiştir. Burke & Sutton (1997) tarafından TLD-100 dozimetreleri için MDD

değeri araştırılmıştır. MDD değeri tavlama ve okuma prosedürlerinin optimize edilmesi ile 80μGy elde edilirken, dekonvolüsyon teknikleri kullanıldığında ise MDD değerinin 10μGy değerine kadar düşürülebildiği gösterilmiştir. Sadek & ark. (2022) tarafından yapılan çalışmaya göre MDD değeri Eşitlik (1)'deki 3σ kuralından farklı olarak yeni bir yöntem önerilerek lüminesans şiddetinin sinyal/gürültü oranı dikkate alınarak araştırılmıştır. Bu çalışmaya göre ±%10 belirsizlikle MDD değerinin 2mGy olabileceği rapor edilmiştir. Meireles & ark. (2013) tarafından TLD-100 için MDD değeri hem fırında tavlama işlemi hemde cihazda TL okuması (TTP) yapılarak farklı tavlama işlemlerinin MDD üzerindeki etkileri araştırılmıştır. Buna göre fırında tavlanan TLD'ler için MDD değeri 3,6 μSv ila 40,0 μSv arasında, TTP tavlama için 7,3 μSv ila 101,3 μSv arasında değişim göstermiştir. Fırında tavlama ile TLD'lerin MDD değerleri daha düşük değerlerde elde edilmiştir. Akter & ark. (2021) tarafından yapılan çalışmada ise TLD-100 dozimetrelerinin artan dozlara (46.82μGy ile 234.1μGy) karşı davranışı ve MDD değeri araştırılmıştır. Sonuçta bu çalışmaya göre MDD değeri 40μGy elde edilmiştir. Bunun haricinde TLD-600 ve TLD-700 için MDD değerinin belirlenmesine yönelik çalışmalar literatürde oldukça sınırlıdır. Ben-Shachar & ark. (1996) tarafından TLD-100, TLD-600 ve TLD-700 kart dozimetreler için MDD değeri grafik yardımıyla belirlenmiştir. Çalışmada kullanılan dozlardaki standart sapmanın %20 değerine sahip olduğu doz değeri MDD kabul edilerek her bir dozimetre türü için MDD belirlenmeye çalışılmıştır. Buna göre TLD-100, TLD-600 ve TLD-700 için MDD değerleri sırasıyla 16.4μGy, 14.3μGy ve 14.7μGy elde edilmiştir.

Bu çalışmada TLD-100, TLD-600 ve TLD-700 dozimetreleri için artan dozlara karşı davranışı ve MDD değerleri araştırılmıştır. MDD ile ilgili olarak literatürdeki çalışmaların çoğunun TLD-100 ile ilgili olduğu görülmüştür. Diğer taraftan TLD-600 ve TLD-700 dozimetreleri ile ilgili çalışmalar literatürde oldukça nadirdir. Bu çalışmada ayrıca MDD değerleri yaygın literatürden farklı olarak sadece toplam alan değeri ile değil aynı zamanda Region of Interest (ROI) kullanılarak TLD-100, TLD-600 ve TLD-700 için her iki duruma göre olası farklılıkların araştırılması hedeflenmiştir.

Materyal ve Metot

Materyal

Bu çalışmada LiF:Mg,Ti (TLD-100), ^{6}LiF:Mg,Ti (TLD-600) ve ^{7}LiF:Mg,Ti (TLD-700) dozimetreleri kullanılmıştır. Dozimetreler Harshaw Chemical Company (ABD)'den satın alınmıştır. Boyutları çip formunda; 3,2×3,2×0,89mm^{3}'dır. TLD-100 ^{6}Li (%7,4) ve ^{7}Li (%92,6) olmak üzere iki elementten oluşmaktadır. Diğer taraftan TLD-600 ve TLD-700 sırasıyla ^{6}Li (%95,6) ve ^{7}Li (%4,4) ile ^{6}Li (%0,1) ve ^{7}Li (%99,9) içermektedir.

Işınlama kaynağı olarak doz hızı 0.92 μGy/s olan Harshaw 2210 Model ^{90}Sr/^{90}Y beta kaynağı kullanılmıştır. TL ölçümleri, WinREMS programı ile kontrol edilen, cam bir filtre, fotoğaltıcı tüp (PMT) ve ısıtma elemanından (planchet) oluşan Harshaw TLD-3500 okuyucu ile gerçekleştirilmiştir. Dozimetrelerin ön ısıtma ve tavlama işlemleri için ise Termo Theldo fırın kullanılmıştır.

Metot

Dozimetreler ölçüm öncesinde ilk olarak tavlama işlemine tabi tutulmuştur. Tüm dozimetreler için uygulanan tavlama ve ön

ısıtma sıcaklıkları aynıdır. Tavlama işlemi, 400°C'de 1 saat ve bunu takiben 100°C'de 2 saat olarak uygulanmıştır. Ön ısıtma işlemi ise 100°C'de 10 dakika uygulanmıştır. Diğer taraftan her dozimetre türü için TL ölçüm protokolü Tablo 1'de sunulmuştur. Olası termal sönüm kaybına uğranmaması ve materyal ile planchet arasında homojen bir ısı transferi sağlamak adına TL ölçümleri en düşük ısıtma hızı olan 1°C/s'lik ısıtma hızlarında gerçekleştirilmiştir. Uygulanan ölçüm protokolü Aşlar (2023)'de verilen ile aynıdır.

Tablo 1: TL ölçüm protokolü

Dozimetre Türü	Ölçüm Sıcaklığı (°C)	Ölçüm süresi (s)
TLD-100	350	300
TLD-600 TLD-700	400	350

MDD değeri, Eşitlik (1) aracılığı ile hem TL ışıma eğrisi altındaki toplam alan hem de Region of Interest (ROI) kullanılarak belirlenmiştir. İlgilenilen ROI aralığı, ışıma eğrisindeki 3.,4. ve 5. pikleri içerecek şekilde 50-120 kanal arası (110-250°C) sıcaklık bölgesi içerisinde kalan alan şiddeti dikkate alınarak belirlenmiştir. Ölçümlerde toplamda 5'er adet dozimetre kullanılmıştır. Şekillerde verilen hata payları, bu 5 dozimetreden elde edilen ortalama sayım değerinden sapmayı ifade etmektedir. En son kısımda MDD değerindeki hata değerleri ise doğal fon sayım değerindeki belirsizlik, kalibrasyon faktöründeki belirsizlikler (ışınlama kaynağı, lüminesans şiddetindeki belirsizlik) dikkate alınarak belirlenmiştir.

Buna ek olarak, dozimetreler farklı dozlarda ışınlanarak dozimetrelerin artan doza karşı davranışı araştırılmıştır. Bu amaç doğrultunda ilk olarak cihazın verebildiği en düşük doz değeri olan 0.05mGy ile 10 mGy doz değeri arasında araştırılmıştır. Aralıktaki

diğer doz değerleri, 1mGy,2mGy ve 5 mGy'dir. Bu doz değerleri için dozimetrelerden elde edilen lüminesans şiddet değerleri, MDD'nin belirlenmesi protokolünde olduğu gibi hem toplam alan hem de ROI kullanılarak araştırılmıştır. Her bir doz için doz cevap eğrileri oluşturulmuştur. Doz cevap eğrilerinin lineerliği eğriler doğrusal bir fonksiyona (y=ax+b) fit edilmesiyle araştırılmıştır. Eğrilerde R^2 değerinin değişimi hem toplam alan hem de ROI için izlenmiştir. Ayrıca bu doz cevap eğrilerinin değişiminin araştırılması sayesinde Eşitlik (1)'deki kalibrasyon faktörü olan ϕ değerinin belirlenmesinde fayda sağlamıştır. Benzer bir çalışmada MDD değeri simülasyon aracılığı ile iki farklı pike sahip olan farklı bir dozimetre türü için Yüksel (2018) tarafından araştırılmıştır.

Bulgular ve Tartışma

TLD-100 Sonuçları

TLD-100 için fırın sonrası 5 adet dozimetreye (D1, .. , D5) ait doğal fon sayım (background) TL şiddet değerlerinin değişimi Şekil 1'de gösterilmiştir. Buna göre ışınlanmamış dozimetreler için bilinen doğal fon sayım grafikleri elde edilmiştir. Artan sıcaklık değeri ile özellikle 250ºC'den sonra lüminesans şiddeti artış göstermiştir. 5 dozimetreden elde edilen ortalama doğal fon sayım değeri (B) değeri toplam alan için 130386, ROI için 17928 bulunmuştur. Bu değerlere karşı gelen standart sapma değerler ise, 12072 ve 1029 olarak elde edilmiştir.

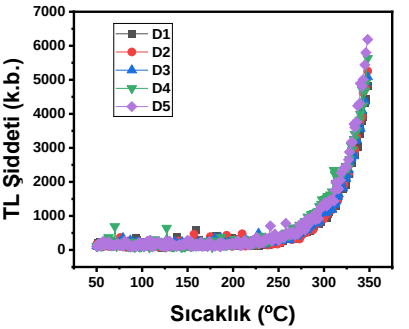

Şekil 1: TLD-100'e ait doğal fon sayım (background) TL ışıma eğrileri

TLD-100 için 0.05 mGy ile 10mGy arasında dozimetrelerin TL ışıma eğrilerinin değişimi ise Şekil 2'de gösterilmiştir. Elde edilen ışıma eğrisi karakteristik olarak TLD-100 ışıma eğrisini göstermektedir. İlk iki pik ön ısıtma işlemi sebebi ile grafikte görülmezken, diğer kalan pikler ışıma eğrisinde görülmektedir. Ayrıca, doz değeri arttıkça 100-250ºC sıcaklık aralığında pikler daha belirgin hale gelerek, lüminesans şiddet değeri artış göstermiştir. Bu değişimin daha iyi anlaşılması için her bir dozdaki lüminesans şiddet değişimi yani doz cevap ilişkisi Şekil 3'de gösterilmiştir. Bu şekilde, 0.05mGy ile 10mGy arasındaki dozlarda ışıma eğrileri altında kalan toplam alan ve ROI durumuna göre elde edilen şiddet değerlerinin değişimleri gösterilmiştir.

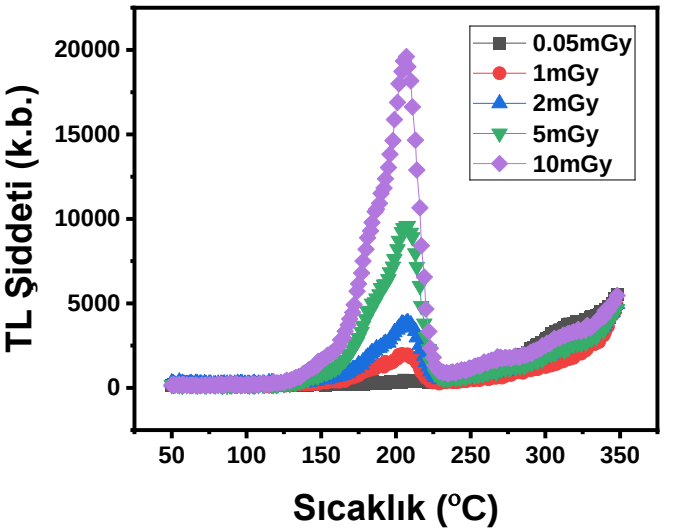

Şekil 2: Farklı radyasyon dozlarına karşı TLD-100 dozimetrelerinin TL ışıma eğrilerinin değişimi

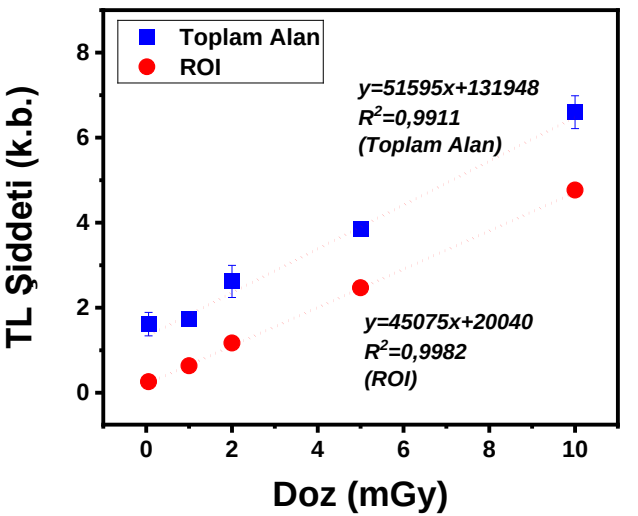

Şekil 3: TLD-100 için toplam alan ve ROI'ye göre elde edilen doz cevap ilişkisi

Şekil 3'ten görüleceği gibi hem toplam alan hem de ROI'ye göre doz arttıkça lüminesans şiddeti artış göstermiştir. Doz cevap eğrileri doğrusal fonksiyona fit edildiğinde R^2 değeri toplam alan için 0,9911; ROI durumunda ise 0,9982 olarak bulunmuştur. Buna göre ROI durumunda elde edilen doz cevap eğrileri toplam alana göre daha iyi sonuç vermiştir. Ayrıca, toplam alan durumunda özellikle başlangıç dozlarındaki hata payları ROI durumuna göre daha yüksektir.

MDD değeri belirlenirken toplam alan durumunda lineerlik için başlangıç dozu 1 mGy, ROI için 0.05mGy alınarak kalibrasyon faktörleri belirlenmiştir. Buna göre, kalibrasyon faktörleri toplam alan için 5.72×10^{-6}mGy, ROI için ise 2.17×10^{-6}mGy olarak bulunmuştur. Sonuçta, MDD değeri ise toplam alana göre 207.27±36.89µGy, ROI için ise 6.70±0.98µGy olarak elde edilmiştir.

TLD-600 Sonuçları

TLD-600 dozimetresi için elde edilen doğal fon sayım (B) değerlerinin TL ışıma eğrileri Şekil 4'de gösterilmiştir. Elde edilen grafikler TLD-100 için elde edilen doğal fon sayımı ile kıyaslandığında TLD-100 için 350ºC olan sıcaklığın TLD-600 için 400ºC'ye yükselmesi ile lüminesans şiddetinde önemli artış gözlenmiştir. Diğer taraftan eğri yapıları benzerdir. 5 dozimetreye göre ortalama B değeri toplam alan için 657522, ROI için ise 26829 olarak edilmiştir. Bu değerlere karşı gelen standart sapma değerleri ise 44201 ve 1861 bulunmuştur.

TLD-600 için 0.05 mGy ile 10mGy arasındaki ışıma eğrilerinin değişimi Şekil 5'de verilmiştir. TLD-100 dozimetresine benzer şekilde piklerin şiddet değerleri, doz arttıkça artış göstermiştir. Diğer taraftan 300ºC sıcaklıktan sonra doğal fon sayım değeri TLD-100 dozimetresine göre daha baskındır. Bir başka deyişle, TLD-600 dozimetresinin dozimetrik pik bölgesi, TLD-100 ile kıyaslandığında doğal fon sayım değerine göre daha düşük şiddette kalmıştır.

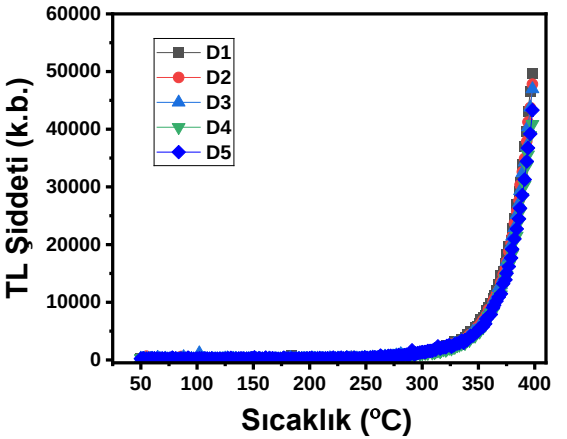

Şekil 4: TLD-600'e ait doğal fon sayım TL ışıma eğrilerinin değişimi

Işıma eğrileri altında kalan alan toplam alan değerleri ve ROI'ye göre belirlenen lüminesans şiddet değerlerinin doza göre değişimi ise Şekil 6'de gösterilmiştir.

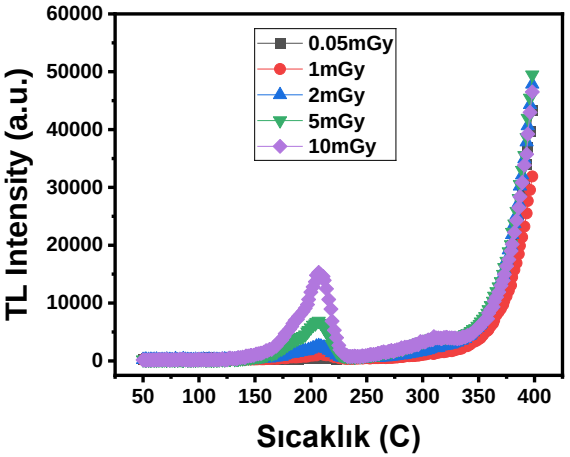

Şekil 5: Farklı radyasyon dozlarına karşı TLD-600 dozimetrelerinin TL ışıma eğrilerinin değişimi

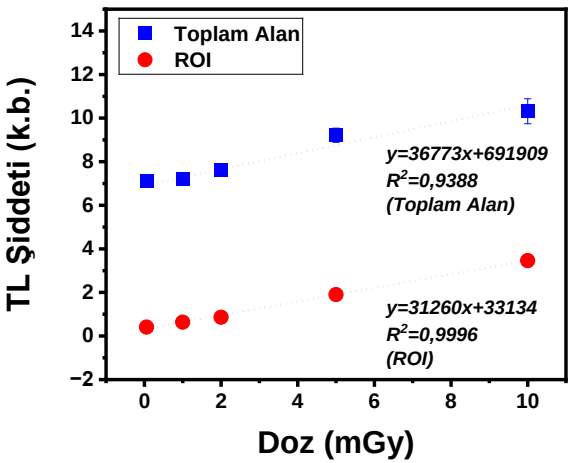

Şekil 6: TLD-600 için toplam alan ve ROI'ye göre doz cevap şiddet değişimi

Şekil 6'dan görüldüğü gibi toplam alan ve ROI'ye göre dozimetrelerin davranışı TLD-100 durumunda olduğu gibi birbirine

göre farklılık göstermiştir. Doz cevap eğrilerinin fit edilmesi sonucunda toplam alan için R^2 değeri 0,9388 iken, ROI durumunda R^2 değeri 0,9996 olarak elde edilmiştir. Sonuç olarak ROI durumunda elde edilen lineerlik toplam alan durumuna göre daha iyi sonuç vermiştir. Bu durum ROI durumunda 350ºC sonrasındaki doğal fon sayım değerinin hesaba katılmaması sayesinde daha kararlı sonuçlar vermesinden kaynaklanmaktadır.

Sonuç olarak, TLD-600 için MDD değeri, toplam alan durumunda 1mGy'deki kalibrasyon faktörü 1.39×10^{-6}mGy dikkate alınarak, ROI için ise 0.05mGy'deki kalibrasyon faktörü 1.35×10^{-6}mGy dikkate alınarak belirlenmiştir. Buna göre MDD değeri toplam alan için 184.54±17.20μGy ve ROI için ise 7.56±1.08μGy olarak elde edilmiştir.

TLD-700 Sonuçları

TLD-700 dozimetresi için elde edilen dozimetrelere ait background (B) değerlerinin TL ışıma eğrileri Şekil 7'de verilmiştir. Şekle göre ışıma eğrileri TLD-600 için elde edilen duruma benzer davranış sergilemişlerdir.

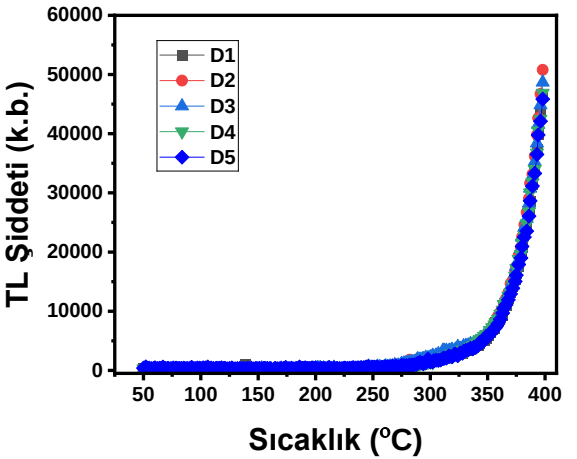

Şekil 7: TLD-700'e ait doğal fon sayım (background) ışıma eğrilerinin değişimi

Buna göre dozimetrelerden elde edilen ortalama B değeri toplam alan için 712781, ROI için 34423 bulunmuştur. Bu değerlere karşı gelen standart sapma değerleri ise, 28553 ve 3119 olarak bulunmuştur. Şekil 8'de ise TLD-700 için 0.05 mGy ile 10mGy doz aralığında TL ışıma eğrilerinin değişimi verilmiştir. TL ışıma eğrilerinin doza göre değişimi yine TLD-600 dozimetresine benzerdir.

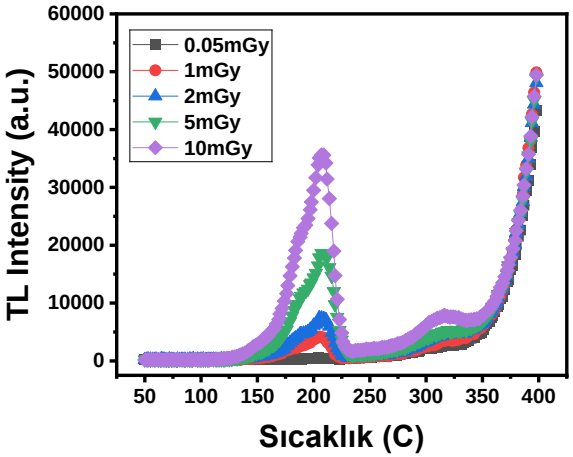

Şekil 8: TLD-700 dozimetrelerinin ışıma eğrilerinin farklı radyasyon dozlarına göre değişimi

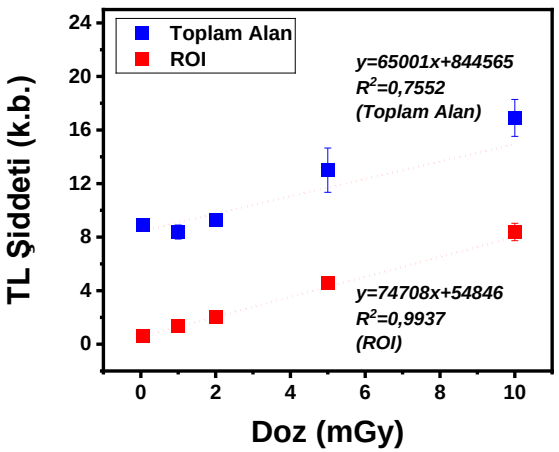

Şekil 9: TLD-700 için toplam alan ve ROI'ye göre doz cevap şiddet değişimi

Şekil 9'da toplam alan ve ROI'ye göre dozimetrelerin artan doza karşı lüminesans şiddetlerindeki değişim verilmiştir. Elde edilen verilerin fit edilmesi sonucunda toplam alan için R^2 değeri 0,7552 iken, ROI için R^2 değeri 0,9993 bulunmuştur. ROI durumunda elde edilen lineerlik toplam alana göre daha iyi sonuç vermiştir. Toplam alan durumunda özellikle ilk doz (0.05mGy) değerinde dozimetrelerden elde edilen şiddet değerlerinin yüksek oluşu lineerlikte daha fazlaya sapmaya yol açmıştır. Kalibrasyon faktörleri toplam alan için 1mGy baz alınarak 1.19×10^{-6} mGy, ROI için 0.05 mGy alınarak 9.11×10^{-7} mGy olarak bulunmuştur. Sonuç olarak TLD-700 için MDD değeri toplam alan için 102.26±11.22µGy ve ROI için ise 8.53±1.32µGy elde edilmiştir.

TLD-100 için bizim çalışmamızda toplam alana göre elde edilen MDD değeri literatürle kıyaslandığında daha yüksektir. Ancak ROI durumuna göre elde edilen MDD değeri Horowitz & Moscowith (1986); Burke & Sutton (1997); Horowitz & ark. (2007) ve Meireles & ark. (2013) ile uyumlu olduğu görülmüştür. Bizim çalışmamızda toplam alan durumuna göre elde edilen değerin yüksek olması, doğal fon sayım değerlerindeki belirsizliğin daha fazla olması ile ilişkili olduğu düşünülmektedir. Ayrıca literatürde TLD-100 dozimetrelerinin ısıtıldığı maksimum ısıtma sıcaklığının farklı olması örneğin daha düşük sıcaklığa ısıtılması MDD değerinin daha düşük olmasına yol açmış olabilir. Diğer taraftan TLD-600 ve TLD-700 için elde edilen MDD değerleri literatürdeki sınırlı çalışma nedeniyle sadece Ben-Shachar & ark. (1996) ile karşılaştırılmıştır. Bizim çalışmamızda toplam alan durumuna göre elde edilen değer yine yüksek bulunurken, ROI durumuna göre elde edilen MDD değerleri Ben-Shachar & ark. (1996) çalışması ile çok iyi bir şekilde

uyumlu bulunmuştur. Toplam alan değerine göre farklılığın olası sebebi, Ben-Shachar & ark. (1996) çalışmasında TLD-600 ve TLD-700 kart dozimetreleri 300ºC'ye ısıtılmasından kaynaklanmaktadır. Bizim çalışmamızda dozimetreler 400ºC'ye ısıtılmıştır. Dozimeterlerin yüksek sıcaklığa ısıtılması sonucu doğal fon sayım değerlerinin dozimetrik pik bölgesine göre daha fazla dalgalanması sigmadaki belirsizlik artarak MDD'nin daha yüksek çıkmasına yol açmıştır. Diğer taraftan, ROI durumunda dozimetrik piklerle ilgilenildiği için MDD değerleri birbirlerine oldukça yakın elde edilmiştir. Bu durum ROI kullanımı ile kararlı MDD değerlerinin belirlenmesinin önemini göstermiştir.

SONUÇLAR

Bu çalışmada dozimetreler için önemli bir deneysel parametre olan MDD değeri TLD-100, TLD-600 ve TLD-700 dozimetreleri için hem toplam alan şiddeti hem de ROI alınarak ayrı ayrı araştırılmıştır. Buna ek olarak dozimetrelerin artan doza karşı davranışları da incelenmiştir. TLD-100 için MDD değeri toplam alana göre 207.27±36.89μGy, ROI için 6.70±0.98μGy olarak bulunmuştur. TLD-600 için MDD değeri toplam alan ve ROI için sırasıyla 184.54±17.20μGy ve 7.56±1.08μGy elde edilmiştir. Son olarak TLD-700 için ise toplam alan ve ROI için 102.26±11.22μGy ve 8.53±1.32μGy olarak bulunmuştur. Görüldüğü gibi bütün durumlarda toplam alana göre elde edilen MDD değeri, ROI kullanılarak elde edilen duruma göre daha yüksek elde edilmiştir. Yani bir başka deyişle, ROI kullanıldığında daha düşük doz değerlerinin ölçülebilmesi mümkün hale gelmiştir. Bu durumun asıl sebebi, düşük dozlarda dozimetrelerin sahip olduğu doğal fon sayım (background) değerinin ışınlanmış olan dozimetreden elde edilen

sayım değerinden ayrıştırılamamasıdır. Özellikle 250ºC sıcaklık değerinden sonra ortaya çıkan siyah cisim ışıması kaynaklı doğal fon sayım değerinin yüksek sıcaklık pik bölgelerinde sinyal artışlarına sebep olmasıdır. ROI alındığında sadece dozimetrik pikler ile ilgilenildiğinden bahsedilen etkilerin minimize edilmesi ile MDD değeri daha aşağı çekilebilmektedir. Elde edilen bu MDD değerleri teorik olarak belirlenen değerler olarak lüminesans dozimetre karakterizasyonunda göreceli olarak dozimetre türlerinin ölçüm kapasitelerini belirleme açısından oldukça önemlidir. Ancak diğer taraftan, doğrudan deneysel olarak bu değerlere ulaşmak sadece dozimetrelerin kendi hassasiyetlerinin sonucu ile değil aynı zamanda ölçüm cihazlarının hassasiyetleri ile de doğrudan ilişkilidir. Örneğin dozimetrelerin tavlama işlemi esnasında kullanılan fırınların hem ısıtma hem de doğru soğutma performansının etkin bir şekilde yapılamaması dozimetrelerin doğrudan doğal fon sayım değerlerini (background) etkileyecek ve MDD değerlerinde beklenilenden farklı sonuçlar verecektir. Yine ışınlama ve ölçüm cihazlarının kalibrasyonlarının MDD değerinin belirlenmesinde önemli etkileri vardır. Ayrıca, ölçüm cihazlarında lüminesans ışık dedeksiyonunun iyileştirilmesi (ölçüm geometri farklılığı vb.) ve/veya TL ışıma eğrilerinde piklerin ayrıştırma teknikleri gibi metotların geliştirilmesi MDD değerini daha aşağı çekerek daha düşük doz değerlerinin ölçülmesini mümkün kılabilir.

KAYNAKÇA

Aitken, M. J. (1985). *Thermoluminescence Dating*. London: Academic Press, 153.

Akter, Y., Rahman, A. M., Sahadath, M. H., Yeasmin, S., Hassan, N., Banik, S., & Hossain, Z. (2022). Thermoluminescence Responses of TLD–100 Subject to Low Dose Irradiation. *Dhaka Univ. J. Appl. Sci. Eng.*, *6*, 59-63.

Aşlar, E. (2023). Investigation of Thermal Quenching Effect for Lithium Fluoride (LiF) Type Dosimeters. *Cumhuriyet Science Journal*, *44*(2), 389-395.

Aznar, M. C., & Hemdal, B. (2008). Absorbed dose measurement in mammography. In *Cancer Imaging* (pp. 493-501). Academic Press.

Ben-Shachar, B., Weinstein, M., & German, U. (1996). Some dosimetric properties of the LiF: Mg, Ti evaluated by the automatic 6600 thermoluminescent reader. *NRC-Negev, P.O.B. 9001*, Beer-Sheva, 84190.

Bos, A. J. (2006). Theory of thermoluminescence. *Radiation measurements*, *41*, S45-S56.

Bos, A. J. J. (2001). High sensitivity thermoluminescence dosimetry. *Nuclear Instruments and Methods in Physics Research Section B: Beam Interactions with Materials and Atoms*, *184*(1-2), 3-28.

Burke, K., & Sutton, D. (1997). Optimization and deconvolution of lithium fluoride TLD-100 in diagnostic radiology. *The British Journal of Radiology*, *70*(831), 261-271.

Cameron, J. R., Zimmerman, D., Kenney, G., Buch, R., Bland, R., & Grant, R. (1964). Thermoluminescent radiation dosimetry utilizing LiF. *Health physics*, *10*(1), 25-29.

Chen, R., & Pagonis, V. (2011). *Thermally and optically stimulated luminescence: a simulation approach*. John Wiley & Sons.

Daniels, F., Boyd, C. A., & Saunders, D. F. (1953). Thermoluminescence as a research tool. *Science*, *117*(3040), 343-349.

Ekinci, F., & Aşlar, E. (2024). Thyroid and contralateral breast surface dose variation in mammography: a phantom study on the role of breast tissue composition. *The European Physical Journal Plus*, 139(4), 330.

Furetta, C. (2010). *Handbook of thermoluminescence*. World Scientific.

Harvey, J. A. (2011). *Performance of Thermoluminescent Dosimeters Under As-Deployed Conditions* (Doctoral dissertation, University of Michigan).

Hirning, C. R. (1992). Detection and determination limits for thermoluminescence dosimetry. *Health physics*, *62*(3), 223-227.

Horowitz, Y. S., & Moscovitch, M. (1986). LiF-TLD in the microgray dose range via computerised glow curve deconvolution and background smoothing. *Radiation Protection Dosimetry*, *17*(1-4), 337-342.

Horowitz, Y. S., Oster, L., & Datz, H. (2007). The thermoluminescence dose–response and other characteristics of the

high-temperature TL in LiF: Mg, Ti (TLD-100). *Radiation protection dosimetry*, *124*(2), 191-205.

Kron, T. (1994). Thermoluminescence dosimetry and its applications in medicine--Part 1: Physics, materials and equipment. *Australasian physical & engineering sciences in medicine*, *17*(4), 175-199.

McKeever, S. W. (1985). *Thermoluminescence of solids* (Vol. 3). Cambridge university press.

McKeever, S. W., Moscovitch, M., & Townsend, P. D. (1995). Thermoluminescence dosimetry materials: properties and uses.

Meireles, L. S., Lacerda, M. A. S., Meira-Belo, L. C., & Ferreira, H. R. (2013*)*. Study of the influence of the time temperature profile on the minimum detectable dose of TLD-100. *International Nuclear Atlantic Conference - INAC 2013*, Brazil, November 24-29.

Rawat, N. S., Dhabekar, B., Kulkarni, M. S., Muthe, K. P., Mishra, D. R., Soni, A., ... & Babu, D. A. R. (2014). Optimization of CW-OSL parameters for improved dose detection threshold in Al2O3: C. *Radiation measurements*, 71, 212-216.

Sadek, A. M. (2020). Uncertainty of thermoluminescence at low dose levels: a Monte-Carlo simulation study. *Radiation Protection Dosimetry*, *192*(1), 14-26.

Sadek, A. M., Abdou, N. Y., & Alazab, H. A. (2022). Uncertainty of LiF thermoluminescence at low dose levels: Experimental results. *Applied Radiation and Isotopes*, *185*, 110245.

Yukihara, E. G., McKeever, S. W., Andersen, C. E., Bos, A. J., Bailiff, I. K., Yoshimura, E. M., ... & Christensen, J. B. (2022). Luminescence dosimetry. *Nature Reviews Methods Primers*, 2(1), 26.

Yüksel, M. (2018). *Termolüminesans Yöntemi ve Dozimetrik Çalışmalar*, Ankara: Nobel Akademik Yayıncılık Eğitim Danışmanlık Tic. Ltd. Şti.

CHAPTER IV

Numerical evaluation of second virial coefficient over Exp-6 potential

Elif SOMUNCU

Introduction

Knowing the physical and chemical properties of atoms and molecules has an important place in scientific and technological research. Many features such as the structure of atomic clusters, interactions between atoms and molecules, thermodynamic properties, potential energy surfaces including regional and global minimum energies of the cluster have been the subject of research. To examine these properties, an equation of state of the form (P, V, T) = 0 is needed, which gives the relationship between the pressure, volume, and temperature of the molecules. To date, studies have been carried out on many real gas equations of state that give the relationships between P-V-T of gases at high pressure.

Many numerical and empirical relations compatible with experimental data have been proposed to describe the P-V-T

behavior of gases and liquids. These proposed equations are equations of state with two or more constants and are very useful. Some of these equations gave quite accurate results in the low temperature and low-density range. However, it is not possible to establish a connection with parameters suitable for intermolecular forces. Therefore, very few methods have been established to connect the basis of intermolecular interactions to gas behavior.

An equation of state that allows finding the thermodynamic properties of gas and liquid molecules was first proposed by Van der Waals (Hirschfelder et al., 1954; McQuarrie and Simon., 1997). To explain the deviations from the ideal gas laws, Van der Waals created the equation of state, considering that the volume of high-density gas molecules is not negligible compared to the ambient volume and that the intermolecular attraction force will cause a decrease in gas pressure. Van der Waals won the Nobel Prize in 1910 for his work on the equation of state of gases and liquids (McQuarrie and Simon., 1997). Along with the Van der Waals equation of state, Dieterici and Berthelot equations of state with two constants have also been proposed (Hirschfelder et al., 1954). These state equations are useful due to their simple analytical form (Hirschfelder et al., 1954). Some of the equations of state proposed later are Battie-Bridgeman (with five constants), Redlich-Kwong, Peng-Robinson, Benedict-Webb-Rubin (with eight constants) (Hirschfelder et al., 1954). Although many equations of state have been proposed to describe the changes between P, V and T of gases and liquids, most of them have been valid in limited cases. Again, many of them cannot meet the conditions that need to be verified in the theory of state equations.

One of the most important state equations that gives the relationship between physical quantities that determine the state variables of physical systems is the virial state equation. Compared to other equations, it is an accurate model for real gases over a wide temperature and pressure range (Hryniewicki, 2011; Shaul et al., 2012). This equation was first proposed by Thiesen and later developed by Kammerlinh-Onnes (Onnes, 1901; Hirschfelder et al., 1954; Mason and Spurling, 1969; McQuarrie, 1973). The original origin of the virial state equation was experimental, but it was later expressed theoretically by considering intermolecular interactions (Mason and Spurling, 1969).

The virial equation, which is the great success of statistical mechanics, is directly linked to intermolecular interaction potentials (Kihara, 1953; Prausnitz et al., 1999; Meng et al., 2006). The virial equation has an important feature that determines the interdependent changes of temperature, pressure, volume, and potential energy of the substance. Virial coefficients in the virial state equation play a fundamental role in many aspects, including the deviation of the gas from the ideal state to the real state and the determination of intermolecular interactions in various temperature ranges (Kihara et al., 1956; Knoebel and Edmister, 1968; Landau et al., 1980; Patria, 1996; McQuarrie et al., 1997; Boltachev and Baidakov, 2006). These coefficients can be applied to all types of molecules, including spherically symmetric or non-symmetric molecules, electrically neutral molecules, polar or non-polar molecules, and complex molecular structures (Prausnitz et al., 1999). At the same time, virial coefficients have an important place in examining the thermodynamic properties of gases (such as internal energy,

enthalpy, heat capacity at constant volume, heat capacity at constant pressure, Joule-Thomson coefficient, speed of sound) and transport properties (viscosity, diffusion, thermal conductivity) (Kihara , 1953; Abdulagatov et al., 2002; Abbaspour and Goharshadi, 2011; Kim et al., 2013). In addition, virial coefficients are used in examining superconductor production and technological application studies, determining the Boyle temperature, and determining the thermodynamic properties of industrial gases and hydrocarbons, which are major energy sources (Kihara, 1953; Glasser, 2002; Viererblova et al., 2010; Oh, 2010; Garberoglio et al. al., 2012; Pai and Bae, 2012). Virial coefficients also have an important place in some areas of biology (Deszczynski et al., 2006; Suzette et al., 2008; Gamez et al., 2011; Quigley et al., 2013).

As can be understood, virial coefficients must be calculated precisely in order to examine atoms and molecules according to the virial equation. Many analytical and numerical methods have been developed to calculate the second virial coefficient from virial coefficients (Pople, 1954; Rice and Hirschfelder, 1954; Konowalow and Hirschfelder, 1961; Sherwood and Prausnitz; 1964; Ragab et al., 1998; Glasser, 2002; Vega et al. ., 2002; Hutem and Boonchui, 2012). However, there are ranges where the formulas created at certain values of the parameters are invalid. As is known from the literature, analytical calculation, and experimental examination of three, four and higher order virial coefficients for different interaction potentials remains one of the important physical problems of today (Haas et al., 1999; MacDowell et al., 2003; Deszczynski et al., 2006; Benjamin et al., 2007; Wheatley, 2013).

Virial Equation of State

Determining the thermodynamic properties, transport properties and interaction potentials of atoms and molecules plays an important role in scientific and technological research (Kihara, 1953; Dymond, 2000; Abdulagatov et al., 2002; Kim et al., 2013; Pai and Bae, 2012; Meng and Duan, 2006; Naresh and Singh, 2009). To accurately explain the thermodynamic properties of molecules, the nature of intermolecular forces must be fully understood (Pai and Bae, 2012). Therefore, many equations of state have been proposed to examine such properties of atoms and molecules. The most suitable equation of state for precise examinations is the virial equation (Shaul and Schultz, 2012). The virial equation, the great achievement of statistical mechanics, is defined following form:

$$\frac{P}{k_B T} = \rho + B_2(T)\rho^2 + B_3(\mathrm{T})\rho^3 + ... \quad (1)$$

Here, $B_2(T)$, $B_3(T)$, … are defined as the second, third, … virial coefficients, respectively (Hirschfelder et al., 1954; McQuarrie, 1973; Chiew and Sabesan, 1999). These coefficients describe the contribution from multi-particle interactions (McQuarrie, 1973; Hutem and Boonchui, 2012; Benjamin et al., 2007). As can be seen from the equation, the N-dimensional problem can be reduced to one, two, three, … dimensional situations in a non-ideal gas (McQuarrie, 1973).

Second Virial Coefficient

The second virial coefficient is very important as it is the first coefficient to depart from the ideal state as the pressure of the gas

increases. This coefficient can be examined theoretically and experimentally (Graben and Present, 1964). The second virial coefficient is written following as (Garberoglio ve ark., 2011):

$$B_2(T) = -2\pi N_A \int_0^{\infty} \left(e^{-u(r)/k_B T} - 1 \right) r^2 dr \qquad (2)$$

Here k_B is Bolztmann constant, N_A is Avogadro constant, and $u(\mathrm{r})$ is intermolecular interaction energy. As can be seen from this equation, the second virial coefficient, which gives the potential energy between two molecules, is physically and chemically related to the intermolecular potential. For pure substances, this coefficient depends on the temperature and the interaction between two molecules (McQuarrie, 1973; Prausnitz, 1999; Naresh and Singh, 2009; Garberoglio et al., 2011). Today, the second virial coefficient is used to examine intermolecular potential models, from the most complex to the simplest. The second virial coefficient takes negative values at low temperatures and positive values as the temperature increases (McQuarrine and Simon, 1997). The temperature when the second virial coefficient is zero is called the Boyle temperature (Kihara, 1953; McQuarrine and Simon, 1997; Estrada-Torres, 2007). At this temperature, intermolecular repulsive and attractive forces are neglected.

Third Virial Coefficient

The third virial coefficient expresses the departure of the gas from the ideal behavior due to the interactions between three molecules (Kihara, 1953; Prausnitz, 1999). This coefficient can be examined experimentally and theoretically (Vega et al., 2002). Third

virial coefficient is defined following form (Hirschfelder et al., 1954):

$$B_3(T) = -\frac{8\pi^2 N_A^2}{3} \iiint f_{12} f_{13} f_{23} r_{12} r_{13} r_{23} dr_{12} dr_{13} dr_{23} \quad (3)$$

In the three-molecular system, there are triple interactions as well as binary interactions. Therefore, working with the third virial coefficients is more difficult than the second virial coefficients (Graben and Present, 1964).

Intermolecular Interaction Potentials

Potential models with simple analytical expressions and determined experimentally are widely used in various physical and chemical problems (Torrens, 1972; Watts and McGee, 1976; Maitland et al., 1987). With the development of high-speed computers, more complex analytical potential functions with many parameters have been used in studies (Kaplan, 2006). Potential functions used in calculating virial coefficients are determined according to the structural properties of atoms or molecules.

Buckingham (Exp-6) Intermolecular Potential

The potential model proposed by Buckingham contains attractive terms due to dipole-dipole dispersion and dipole-quadrupole interactions. The pushing term is expressed with an exponential function. Due to its experimental terms, it is very difficult to work with this potential in practical calculations. The potential includes four parameters. This potential can be written as follows:

$$u(r)=\begin{cases}\dfrac{1}{1-(6/\alpha)}\{\dfrac{6}{\alpha}Exp[\alpha(1-\dfrac{r}{r_m})]-(\dfrac{r}{r_m})^6\} & r>r_{\max}\\ \infty & r<r_{\max}\end{cases} \quad (4)$$

α indicates exponential repellency. ε is the minimum energy value. r_m is the minimum region (Hirschfelder et al., 1954; Prausnitz, 1999). This formula is used to determine the alpha coefficient required to calculate virial coefficients (Hirschfelder et al., 1954):

$$\left(\frac{r_{\max}}{r_m}\right)^7 Exp\left[\alpha\left(1-\frac{r_{\max}}{r_m}\right)\right]=1 \quad (5)$$

Theoretical Evaluation of Second Virial Coefficient with Exp-6 Potential

Potential functions used in calculating virial coefficients are determined according to the structural properties of atoms or molecules. In this study, an analytical expression was created to calculate the second virial coefficient using the Exp-6 potential for some atoms and molecules (Mamedov and Somuncu, 2015). The analytical formula has been obtained following as (Mamedov and Somuncu, 2015):

$$B(\mathrm{T}^*)=6\left(\frac{\sigma}{r_m}\right)^{-3} \mathrm{e}^{\frac{-6}{T^*(\gamma-6)}\mathrm{e}^{\gamma}} \lim_{n\to\infty}\sum_{n=0}^{N}\left(\frac{\gamma}{T^*(\gamma-6)}\right)^{n+1} I(\gamma,\mathrm{T}^*,\rho) \quad (6)$$

In this paper, the second virial coefficient $B(T^*)$ using the alternative formula for $0.02<T^*<0.2$ can be calculate in the following form:

$$B_2(T^*) = -6\left(\frac{\sigma}{r_m}\right)^{-3}\left\{\begin{array}{l} -\dfrac{1}{T^*\gamma^3(\gamma-6)}e^{\frac{-6}{T^*(\gamma-6)}e^{\gamma}+\gamma} \\ \left\{\left(\dfrac{T^*(\gamma-6)}{6}\left(\left(C+\ln\dfrac{6}{T^*(\gamma-6)}\right)^3+\dfrac{\pi^2}{2}\left(C+\ln\dfrac{6}{T^*(\gamma-6)}\right)+2\zeta(3)\right)\right)\right. \\ \left.-K(\gamma,T^*,\rho)\right\} \\ -e^{\frac{-6}{T^*(\gamma-6)}e^{\gamma}}\lim\limits_{n\to\infty}\sum\limits_{n=1}^{N}\dfrac{1}{n!}\left(\dfrac{\gamma}{T^*(\gamma-6)}\right)^{n+1}\left(e^{\gamma}L(\gamma,T^*,\rho)+M(\gamma,T^*,\rho)\right) \end{array}\right\} \quad (7)$$

where $T^* = k_B T/\varepsilon$ and $\rho = r_{\max}/r_m$. The $I(\gamma,\mathrm{T}^*,\rho), K(\gamma,T^*,\rho)$, $L(\gamma,T^*,\rho)$ and $M(\gamma,T^*,\rho)$ functions is defined following form:

$$I(\gamma,\mathrm{T}^*,\rho) = \int_{\rho}^{\infty} \mathrm{e}^{\frac{-6}{T^*(\gamma-6)}\mathrm{e}^{-\gamma r}}\left(r^{-6n+3}\mathrm{e}^{\gamma(1-r)} - r^{-4n-4}\right)dr$$

(8)

$$K(\gamma,T^*,\rho) = \int_{0}^{e^{-\gamma\rho}} e^{\frac{-6\,r}{T^*(\gamma-6)}})\ln r^3 dr \quad (9)$$

$$L(\gamma,T^*,\rho) = \int_{\rho}^{\infty} e^{\frac{-6\,e^{-\gamma r}}{T^*(\gamma-6)}-\gamma r} r^{-6n+3}dr \quad (10)$$

$$M(\gamma,T^*,\rho) = \int_{\rho}^{\infty} e^{\frac{-6}{T^*(\gamma-6)}e^{-\gamma r}} r^{-6n-4}dr \quad (11)$$

The calculation results obtained according to the Buckingham potential were compared with the calculation results obtained according to the Lennard-Jones potential and were found to be compatible with the literature (Hutem and Boonchui, 2012; Mason and Rice, 1954; Rice and Hirschfelder, 1954; Whalley and

Schnider, 1955; Sherwood and Prausnitz, 1964). The potential parameters given in Tables 1-2.

Table 1 The parameters for σ/r_m *(Hirschfelder et al., 1954; Sherwood and Prausnitz; 1964; Prausnitz, 1999)*

γ	σ/r_m
12	0.87610
12.5	0.87983
13	0.88320
13.5	0.88627
14	0.88910
14.5	0.89173
15	0.89417
16	0.898607
18	0.906096
22	0.917442
24	0.921911
30	0.932341
100	0.970041
300	0.986692
∞	1.000000

Table 3. *The potential parameters (Mason and Rice, 1954; Whalley and Schnider, 1955; Konowalow and Hirschfelder, 1961; Kim et al., 2013)*

	Lennard - Jones (12-6)		Exp-6		
Molecules	σ (A)	$\varepsilon/k_B T$ (K)	γ	r_m (A)	$\varepsilon/k_B T$ (K)
He	2.869	10.22	12.4	3.135	9.16
Ar	3.87	119.3	14	3.866	123.2
Kr	4.04	159	12	4.056	158.3
Xe	4.46	228	13	4.450	231.2
N_2	4.16	95.9	16.2	4.040	113.5
CH_4	3.741	160.3	15	4.184	160.3
C_2H_6	3.679	129.6	16	4.094	129.6
CF_4	4.744	151.5	300	4.153	403.6

Table 3. *Comparison of calculated second virial coefficients for Hg* ($N = 50$ *and* $N' = 100$)

T	Eq. (7)	Eq.(6)	(Mamedov and Somuncu, 2014)
25	-1.34388×10^{14}	-1.34388×10^{14}	$-1.342728486\times10^{14}$
26	-3.68948×10^{13}	-3.68948×10^{13}	-3.70204×10^{13}
27	-1.118×10^{13}	-1.118×10^{13}	-1.12381×10^{13}
28	-3.69381×10^{12}	-3.69381×10^{12}	-3.71753×10^{12}
29	-1.31983×10^{12}	-1.31983×10^{12}	-1.32818×10^{12}
30	-5.05273×10^{11}	-5.05273×10^{11}	-5.08564×10^{11}
35	-9.54084×10^{9}	-9.54084×10^{9}	-9.60763×10^{9}
40	-4.91182×10^{8}	-4.91182×10^{8}	-4.94831×10^{8}
45	-4.93023×10^{7}	-4.93023×10^{7}	-4.96901×10^{7}
50	-7.89211×10^{6}	-7.89211×10^{6}	-7.95771×10^{6}
55	-1.77315×10^{6}	-1.77315×10^{6}	-1.7887×10^{6}
60	-513552	-513549	-518299
65	-180787	-180784	-182545
70	-74177.2	-74174.7	-74935
80	-17620.1	-17617.7	-17817.3
90	-5829.32	-5826.93	-5899.75
100	-2431.38	-2429.04	-2462.44
200		-57.8834	-59.4616
300		-17.7838	-18.4331
400		-9.4465	-9.84855
500		-6.14917	-6.43926
600		-4.42474	-4.65105
700		-3.37401	-3.55907
800		-2.66978	-2.82592
900		-2.16622	-2.30091
1000		-1.78896	-1.90708
1200		-1.26267	-1.3568
1400		-0.91421	-0.991724
1600		-0.667346	-0.732616
1800		-0.667346	-0.539698
2000		-0.342539	-0.39084
2400		-0.140025	-0.176994
2600		-0.0653544	-0.0979259
2800		-0.00288736	-0.0316573
3000		0.0500317	0.0245891
3400		0.134509	0.114639
3800		0.198573	0.183212
4000		0.225011	0.211607
4400		0.269436	0.259484
4600		0.288216	0.279798
4800		0.30512	0.298128
5000		0.320391	0.31473

Table 4. *Comparison of calculated second virial coefficients for* CH_4 ($N = 50$ *and* $N' = 100$)

T	Eq. (7)	Eq.(6)	(Mamedov and Somuncu, 2014)
5	-4.35536×10^{12}	-4.35536×10^{12}	$-1.706326101\times10^{12}$
6	-2.94573×10^{10}	-2.94573×10^{10}	$-1.355981161\times10^{10}$
7	-8.4245×10^{8}	-8.4245×10^{8}	-4.350727748×10^{8}
8	-5.92246×10^{7}	-5.92246×10^{7}	-3.334875946×10^{7}
9	-7.57643×10^{6}	-7.57643×10^{6}	-4.563992931×10^{6}
10	-1.47287×10^{6}	-1.47287×10^{6}	-936647.1092
11	-388029	-388027	-257995.5448
12	-128364	-128361	-88591.35194
13	-50583.2	-50580.7	-36037.34749
14	-22867.9	-22865.4	-16744.48098
15	-11538.3	-11535.9	-8652.998661
16	-6364.96	-6362.57	-4874.734267
17	-3778.63	-3776.26	-2948.355705
18	-2384.68	-2382.34	-1891.819158
19	-1584.44	-1582.12	-1275.728759
20	-1099.75	-1097.45	-897.2942005
40		-40.3781	-37.68295465
50		-21.4114	-20.44988304
60		-13.8365	-13.40019001
70		-9.95254	-9.726868384
80		-7.63975	-7.514355431
90		-6.12105	-6.049083897
100		-5.05342	-5.012251467
200		-1.46069	-1.472452181
300		-0.596478	-0.6059437286
400		-0.216924	-0.2224864686
500		-0.00730431	-0.009512999456
600		0.123643	0.1242186986
700		0.212003	0.2149267947
800		0.274852	0.2797975914
900		0.321291	0.3280104460
1000		0.356602	0.3649013121
1200		0.4167883248	0.4167883248
1400		0.437301	0.4506250391
1600		0.458371	0.4736912544
1800		0.472802	0.4898902864
2000		0.482813	0.5014893384
2400		0.494545	0.5159902330
2600		0.497736	0.5204062435
2800		0.499748	0.5235579530
3000		0.500871	0.5257462540
3400		0.501231	0.5280528312
3600		0.500741	0.5284566364
3800		0.499931	0.5284958023
4000		0.498871	0.5282432609
4400		0.496199	0.5270804823
4600		0.494663	0.5262511952
4800		0.493031	0.5252979770
5000		0.491326	0.5242444480

Table 5. *Comparison of calculated second virial coefficients for* Kr $(N = 50 \text{ and } N' = 100)$

T	Eq. (7)	Eq.(6)	(Mamedov and Somuncu, 2014)
6	-8.37391×10^{10}	-8.37391×10^{10}	-8.15807×10^{10}
7	-2.09726×10^{9}	-2.09726×10^{9}	-2.01323×10^{9}
8	-1.33601×10^{8}	-1.33601×10^{8}	-1.26715×10^{8}
9	-1.58291×10^{7}	-1.58291×10^{7}	-1.48747×10^{7}
10	-2.89378×10^{6}	-2.89377×10^{6}	-2.69949×10^{6}
11	-724904	-724901	-672266
12	-229920	-229917	-212201
13	-87422.1	-87419.1	-80363.9
14	-38325.4	-38322.4	-35113.6
15	-18826.8	-18823.8	-17200.2
16	-10143.8	-10140.9	-9244.79
17	-5897.46	-5894.6	-5363.31
18	-3650.17	-3650.17	-3315.8
19	-2386.69	-2383.9	-2162.6
20	-1631.6	-1628.83	-1475.98
25	-396.654	-394.009	-355.945
30		-157.838	-142.504
40		-52.2453	-47.2227
50		-27.1421	-24.5628
60		-17.3618	-15.7198
70		-12.4284	-11.2506
80		-9.52433	-8.61489
90		-7.63345	-6.89588
100		-6.31273	-5.6934
200		-1.92817	-1.68418
300		-0.888502	-0.72638
400		-0.433448	-0.305023
500		-0.182293	-0.0713723
600		-0.0253053	0.0753727
700		0.0807705	0.175024
800		0.156366	0.246419
900		0.212358	0.299601
1000		0.255055	0.340403
1200		0.314795	0.39805
1400		0.353444	0.435923
1600		0.379547	0.461972
1800		0.397676	0.480463
2000		0.410483	0.493878
2400		0.426074	0.511066
2600		0.43062	0.516503
2800		0.448892	0.520523
3000		0.450813	0.523458
3400		0.452366	0.526982
3600		0.452321	0.527888
3800		0.45188	0.528373
4000		0.451126	0.528519
4400		0.448921	0.528037
4600		0.44756	0.5275
4800		0.446073	0.526814
5000		0.444486	0.526004

Acknowledgment

The Scientific and Technological Research Council of Turkey (TUBITAK) (Project No: 114F015) and Gaziosmanpasa University BAP (Project No: 2014/24) have provided financial support for this work.

References

Abbaspour, M. & Goharshadi. E. K. (2010). Computation of Some Thermodynamics, Transport. Structural Properties. and New Equation of State for Fluid Neon Using a New Intermolecular Potential from Molecular Dynamics Simulation. *Theoretical Chemistry Acc*uounts 127 (5/6), 573-585. Doi: 10.1007/s00214-010-0751-5

Abdulagatov, A. I., Kaplun. A. B., Meshalkin, A. B., Abdulagatov, I. M. & Stepanov, G. V. (2002). Second Caloric Virial Coefficients for Real Gases and Combined Spherical Symmetric Potential for Simple Molecular Interactions. *Journal of Chemical Therm*odynamics 34 (12), 2049–2072. Doi: 10.1016/S0021-9614(02)00259-8.

Benjamin, K. M., Singh, J. K., Schultz, A. J. & Kofke, D. A. (2007). Higher-Order Virial Coefficients of Water Models. *Journal of Physical Chemistry B* 111 (39), 11463-11473. Doi: 10.1021/jp0710685

Boltachev, G. S. & Baidakov, V. G. (2006). The Second Virial Coefficients of Simple Fluids. *High Temperature* 44 (1), 83-90. Doi: 10.1007/s10740-006-0009-z

Chiew, Y. C. & Sabesan, V. (1999). Second Virial Coefficients of Lennard–Jones Chains. *Fluid Phase Equilibria* 155, 75-83. Doi: 10.1016/S0378-3812(98)00457-9

Deszczynski, M., Harding, S. E. & Winzor, D. J. (2006). Negative Second Virial Coefficients as Predictors of Protein Crystal Growth: Evidence from Sedimentation Equilibrium Studies that

Refutes the Designation of Those Light Scattering Parameters as Osmotic Virial Coefficients. *Biophysical Chemistry* 120 (2), 106 – 113. Doi: 10.1016/j.bpc.2005.10.003

Dymond, J. H. (2000). Second virial coefficients and liquid transport properties at saturated vapor pressure of haloalkanes. *Fluid Phase Equilibria* 174, 13-32. Doi: 10.1016/S0378-3812(00)00414-3

Estrada-Torres, R., Iglesias-Silva, G. A., Ramos-Estrada, M. & Hall, K. R. (2007). Boyle Temperatures for Pure Substances. *Fluid Phase Equilibria* 258 (2), 148-154. Doi: 10.1016/j.fluid.2007.06.004

Gamez, F., Lago, S., Plaza-Reyes, A. & Gonzalez-Claderon, A. (2011). Second Virial Coefficients of Mesogenic International Potentials. *Journal Molecular Liquids* 164 (1-2), 153-156. Doi: 10.1016/j.molliq.2011.07.009

Garberoglio, G., Moldever, M. R. & Harvey, A. H. (2011). Improved First-Principles Calculation of the Third Virial Coefficient of Helium. *Journal of Research NIST* 116 (4), 729-742. Doi: 10.6028/jres.116.016

Garberoglio, G., Jankowski, P., Szalewicz, K. & Harvey, A. H. (2012). Second Virial Coefficients of H_2 and its isotopologues from a six-dimensional potential. *Journal of Chemical Physics* 137 (15), 154308- 154319. Doi: 10.1063/1.4757565

Glasser, M. L. (2002). Second virial coefficient for a Lennard-Jones ($2n-n$) system in d dimensions and confined to a

nanotube surface. *Physics Letters A* 300 (4-5), 381-384. Doi: 10.1016/S0375-9601(02)00814-9

Graben, H. W. & Present, R. D. (1964). Third Virial Coefficient for the Sutherland (∞, ν) Potential. *Reviews of Modern Phys*ics 1025-1033. Doi: 10.1103/RevModPhys.36.1025

Haas, C., Drenth, J. & Wilson, W. W. (1999). Relation between the Solubility of Proteins in Aqueous Solutions and the Second Virial Coefficient of the Solution. *Journal of Physical Chemistry B* 103 (14), 2808-2811. Doi: 10.1021/jp984035l

Hirschfelder, J. O., Curtiss, C. F. & Bird, R. B. (1954). *Molecular Theory of Gases and Liquids*. New York: Jonh Wiley &Sons.

Hryniewicki, M. K. (2011). *Accurate and Efficient Evaluation of the Second Virial Coefficient Using Practical Intermolecular Potentials for Gases*. Toronto: (Master) University of Toronto Institue for Acrospace Studies.

Hutem, A. & Boonchui, S. (2012). Numerical Evaluation of Second and Third Virial Coefficients of Some Inert Gases via Classical Cluster Expansion. *Journal of Mathematical Chemistry* 50 (5), 1262-1276. Doi: 10.1007/s10910-011-9966-5

Kaplan, I. G. (2006). *Intermolecular Interactions: Physical Picture. Computational Methods and Model Potentials*. New York: Jonh Wiley & Sons.

Kihara, T. (1953). Virial Coefficients and Models of Molecules in Gases. *Reviews of Modern Physics* 25 (4), 831-843. Doi: 10.1103/RevModPhys.25.831

Kihara, T., Midzuno, Y. & Kaneko, S. (1956). Virial Coefficients and Intermolecular Potential for Small Nonspherical Molecules. *Journal of the Physical Society Japan* 11 (4), 362-366. Doi:10.1143/JPSJ.11.362

Kim, H. M., Schultz, A. J. & Kofke, D. A. (2013). Second Through Fifth Virial Coefficients for Models Methane-Ethane Mixtures. *Fluid Phase Equilibria* 351 69-73. Doi: 10.1016/j.fluid.2012.10.014

Knoebel, D. H. & Edmister, W. C. (1968). Second Virial Coefficients of binary Mixtures of Benzene with Methanol, Ethanol, Acetone, and Diethyl Ether. *Journal Chemical Engineering Data* 13 (3), 312–317. Doi: 10.1021/je60038a005

Konowalow, D. D. & Hirschfelder, J. O. (1961). Intermolecular Potential Functions for Nonpolar Molecules. *Physical Fluids* 4 (5), 629-635. Doi: 10.1063/1.1706373

Landau, L. D. & Lifshitz, E. M. (1980). *VII. Non-Ideal Gases. Statistical Physics*. USA: Pergamon.

MacDowell, L. G., Menduina, C., Vega, C. & Miguel de E. (2003). Third Virial Coefficient and Critical Properties of Quadrupolar Two Center Lennard-Jones Model. *Physical Chemistry Chemical Phys*ics 5 (13), 2851-2857. Doi: 10.1039/B302780E

Maitland, G. C., Rigby, M., Smith, E. B. & Wakeham, W. A. (1987). *Intermolecular Forces*. Oxford: Clarendon Press.

Mamedov, B. A. & Somuncu E. (2014) Analytical treatment of second virial coefficient over Lennard-Jones (2n− n) potential and

its application to molecular systems. *Journal of Molecular Structure* 1068, 164-169. Doi: 10.1016/j.molstruc.2014.04.006

Mamedov, B. A., & Somuncu, E. (2015). Accurate calculation of second virial coefficient of the Exp-6 potential and its application. *Physica A: Statistical Mechanics and its Applications, 420,* 246-257. Doi: 10.1016/j.physa.2014.11.014

Mason, E. A. & William, E. R. (1954). The Intermolecular Potentials of Helium and Hydrogen. *J. Chem. Phys.* 22 522-535.

Mason, E. A. & Spurling, T. H. (1969). *The Virial Equation of State*. New York: Pergamon.

McQuarine, D. A. (1973). *Statistical Mechanics*. New York: Harper & Row.

McQuarine, D. A. & Simon, J. D. (1997). *Physical Chemistry: A Molecular Approach*. New York: University Science Book.

Meng, L. & Duan, Y. Y. (2006). Site-Site potential function and second virial coefficients for linear molecules. *Molecular Phys*ics 104 (18), 2891-2899. Doi: 10.1080/00268970600867338

Naresh, D. J. & Singh, J. K. (2009). Virial coefficients and inversion curve of simple and associating fluids. *Fluid Phase Equilibria* 279 47-55. Doi: 10.1016/j.fluid.2009.01.015

Oh, S. K. (2010). Extending the Group Contribution Concept Using Kihara Potential to Perfluorinated n-alkanes $C_nF_{2n+2}\left(n=1-6\right)$ for Estimating Thermophysical. *Fluid Phase Equilibria* 288 87-95. Doi: 10.1016/j.fluid.2009.10.023

Onnes, H. K. (1901). *Expression of the Equation of State of Gases and Liquids by Means of Series*. Commun. Phys. Lab. Leiden.

Pai, S. J. & Bae, Y. C. (2012). Understanding physical properties of hydrocarbon polymers using an equation of state developed from semi soft-core potential function. *Fluid Phase Equilibria* 317 15-24. Doi: 10.1016/j.fluid.2011.12.020

Patria, R. P. (1996). *Statistical Mechanics of Interacting Systems: The Method of Cluster Expansion. Statistical Mechanics*. New York: Elsevier.

Pople, J. A. (1954). The Statistical Mechanic of Assemblies of Axially Symmetric Molecules: II Second Virial Coefficients. *Proceedings of the Royal Society of London. Series A Mathematical and Physical Sciences* 221 508-516. Doi: 10.1098/rspa.1954.0045

Prausnitz, J. M., Lichtenthaler, R. N. & Azevedo, E. G. de (1999). *Fugacities in Gas Mixtures. Molecular Thermodynamics of Fluid-Phase Equilibria.* New Jersey: Prentice-Hall.

Quigley, A., Heng, J. Y. Y., Liddell, J. M. & Williams, D. R. (2013). The Accurate Measurement of Second Virial Coefficients Using Self-İnteraction Chromatography: Experimental Consideration. *European Journal of Pharmaceutics and Biopharmaceutics* 85 (3), 1103-1111. Doi: 10.1016/j.ejpb.2013.04.004

Ragab, S. F., Helmy, A. A., Hassanein, T.L. & El-Naggar, M. A. (1998). A Closed Form for the Second Virial Coefficient Using the Modified Buckingham Potential. *Journal of Low Temperature Physics* 111 (3/4), 447-452. Doi: 10.1023/A:1022212525635

Rice, W. E. & Hirschfelder, J. O. (1954). Second Virial Coefficients of Gases Obeying a Modified Buckingham (Exp-6) Potential. *Journal of Chemical Physics* 22 (2), 187-192. Doi: 10.1063/1.1740027

Shaul, K. R. S., Schultz, A. J., Kofke, D. A., (2012). Path-integral Mayer-sampling calculations of the quantum Boltzmann contribution to virial coefficients of helium-4. *Journal of Chemical Physics* 137 184101-184112. Doi: 10.1063/1.4764857

Sherwood, A. E. & Prausnitz, J. M., (1964). Third Virial Coefficients for the Kihara. Exp-6. and Square-Well Potentials. *Journal of Chemical Physics* 41 (2), 429-437. Doi: 10.1063/1.1725883

Suzette, L.L., Pabit, A., Lamb, J. S., Park, H. Y. & Pollack, L. (2008). Closing the Lid on DNA end-to-end Stacking Interactions. *Applied Physics Letters* 92 (22), 223901-223903. Doi: 10.1063/1.2937402

Torrens, I. M. (1972). *Interatomic Potentials*. New York: Academic Press.

Vega, C., McBridge, C. & Menduina, C. (2002). The Second Virial Coefficient of the Dipolar Two Center Lennard-Jones Model. *Physical Chemistry Chemical Physics* 4 (13), 3000-3007. Doi: 10.1039/b200781a

Viererblova, L., Kolafa, J., Labik, S. & Malijevsky, A. (2010). Virial Coefficients and Equation of State of the Penetrable Sphere Model. *Physical Chemistry Chemical Physics* 12 (1), 254-262. Doi: 10.1039/B917204A

Watts, R. O. & McGee, I. G. (1976). *Liquid State Chemical Physics*. New York: John Wiley & Sons.

Whalley, E. & Schnider, W. G. (1955). Intermolecular Potentials of Argon. Krypton. and Xenon. *J. Chem. Phys*. 23 1644-1650. Doi: 10.1063/1.1742403

Wheatley, R. J. (2013). Calculation of Higher-Order Virial Coefficients with Applications to Hard and Soft Spheres. *Physical Review Lett*ers 110 200601-200604. Doi: 10.1103/PhysRevLett.110.200601

CHAPTER V

Investigation of spectroscopic properties of Cu(II)-Acetazolamide/Nicotinamide complex by computational chemistry method: Molecular Modelling Study, ADME and Toxicology

Filiz ÖZTÜRK[1]
Tuğba AYCAN[2]

Introduction

Acetazolamide (acm: N-(5-sulfamoyl-1,3,4-thiadiazol-2-yl)acetamide) inhibits carbonic anhydrase, which catalyzes the hydration of carbon dioxide and the dehydration of carbonic acid. Acetazolamide is the first mercury-free drug with a diuretic effect (Bertini, Gray, Lippard, & Valentine, 1994). Later, it was used for clinical purposes for the treatment of glaucoma, epilepsy, and other

[1] Doç. Dr., Ondokuz Mayıs University, Karadeniz Advanced Technology Research and Application Center, , Samsun/Turkey, Orcid: 0000-0002-0493-0446 filiz.ozturk@omu.edu.tr
[2] Doç. Dr., Sinop University, Faculty of Arts and Sciences, Department of Physics, Sinop/Turkey, Orcid: 0000-0002-5313-7807, tugba.aycan84@gmail.com

neuromuscular diseases (Akocak et al., 2017; Saczewski et al., 2006; Scozzafava & Supuran, 2014; Singh et al., 2020; Supuran, 2012; Supuran, Casini, & Scozzafava, 2004). There is a great interest in the synthesis of structural derivatives to improve the inhibitory activity and pharmacological activities of acetazolamide, which is an enzyme inhibitor with a therapeutic effect (they slow down the reaction by temporarily or completely inactivating enzymes) (Diaz et al., 2016; Health, 2002).

Computational vibration frequencies (FT-IR), optimized molecular geometric parameters, HOMO-LUMO analyzes of the $[Cu(Hacm)_2(na)_2(H_2O)_2]$ complex, which were experimentally studied by Öztürk et al., were investigated (Öztürk, Bulut, Paşaoğlu, Bulut, & Büyükgüngör, 2012). Theoretical calculations were made using the LanL2DZ basis set and the B3LYP functional in the DFT method. By utilizing the calculated HOMO and LUMO energy values, we were able to determine various molecular properties including ionization potential, electron affinity, electronegativity, chemical hardness, chemical softness, chemical potential, and electrophilic index parameters. All these interactions were visualized and verified using Hirshfeld surface analysis. Molecular docking studies were performed against the DHPS of Yersinia pestis with AutoDockVina software.

Computational methods

For the theoretical calculations of the $[Cu(Hacm)_2(na)_2(H_2O)_2]$ complex, Gaussian-09 and GaussView-5.0 software and DFT (Density functional theory)-B3LYP hybrid method were used (Becke, 1993; Dennington II, Keith, & Millam, 2009; M. Frisch et al., 2014; Lee, Yang, & Parr, 1988). For the

optimization of the complex and IR vibrations, calculations were made using the LanL2DZ basis set (Check et al., 2001; Chiodo, Russo, & Sicilia, 2006) and the 6-311G basis set for the Acetazolamide ligand (M. J. Frisch, Pople, & Binkley, 1984). TD-SCF method 6-311G basis sets were used to calculate the electronic transitions of the copper complex. Orbital energies, vibration energies, and transition energies were displayed with the help of GaussSum software (O'boyle, Tenderholt, & Langner, 2008). Hirshfeld surface analysis was performed with a single crystal CIF file. Crystal Explorer 17.5 software was used for this analysis (Turner et al., 2017). The DHPS of Yersinia pestis was downloaded from PDB (Protein Data Bank) (PDB ID: 3TZF http://www.rcsb.org./pdb). Molecular modeling studies were performed with AutoDock Tool (ADT) v1.5.6 and AutoDock Vina docking software (Trott & Olson, 2010). Polar hydrogen atoms were added by ignoring the waters of the enzymes with the ADT software. Grid is created at 1Å intervals. Interactions between the complex and enzymes were listed and visualized using DS (Discovery Studio) software (D. S. BIOVIA). The drug-similarity properties of the compounds were performed by the SwissADME web server. Effective drug research requires studying ADME parameters (Adsorption, Distribution, Metabolism, Excretion) and pharmacokinetic properties of small compounds, such as drug similarity (Daina, Michielin, & Zoete, 2017). OpenBabelGui and SwissADME were used to analyze the compounds' pharmacokinetic properties (Norinder & Bergström, 2006). In addition, the ProTox-II free web server (https://tox-new.charite.de/protox_II/) was utilized to predict various toxicological features of these chemical

compounds (Banerjee, Dehnbostel, & Preissner, 2018; Banerjee, Eckert, Schrey, & Preissner, 2018; Drwal, Banerjee, Dunkel, Wettig, & Preissner, 2014). The drug toxicity study aims to provide accessibility, accuracy, and speed.

Result and Discussions

Geometry optimization

The X-ray diffraction view (Öztürk et al., 2012) and the optimized structure view of the [Cu(Hacm)$_2$(na)$_2$(H$_2$O)$_2$] complex are given in Figure 1a,b. Theoretical DFT/B3LYP/LANL2DZ and X-ray diffraction data of some selected geometric parameters of the studied molecule (Öztürk et al., 2012) are given comparatively in Table 1.

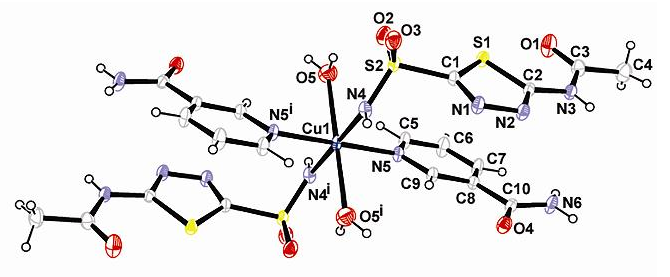

(a)

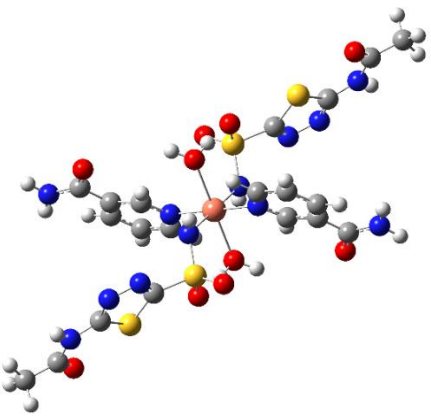

(b)

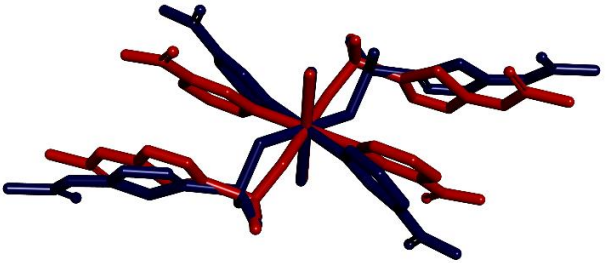

(c)

Figure 1: a) X-ray diffraction (Öztürk et al., 2012) and b) optimized structure view and c) superimpose the image of the studied complex

Table 1: Bond lengths (Å) and Bond angles (°) for $Cu(Hacm)_2(na)_2(H_2O)_2$.

Bond Lengths	XRD(Öztürk et al., 2012)	DFT
Cu1—N4	2.0147 (16)	2.0365
Cu1—N4^{i}	2.0147(16)	2.0365
Cu1—N5	2.0490(16)	2.0800
Cu1—N5^{i}	2.0490(16)	2.0800
Cu1—O5	2.5021(19)	2.4568
S2—O2	1.4390(13)	1.6291
S2—O3	1.4443(15)	1.6532
S2—N4	1.5430(16)	1.7289
N3—C3	1.364(2)	1.3887
N3—C2	1.376(2)	1.3981
N6—C10	1.325(2)	1.3783
C1—N1	1.290(2)	1.3047
N1—N2	1.372(2)	1.4064
C2—N2	1.297(2)	1.3329
Bond Angles		
N4—Cu1—N4^{i}	180.00(14)	180
N4—Cu1—N5	91.27(6)	91.947
N4^{i}—Cu1—N5	88.73(6)	88.053
N4—Cu1—N5^{i}	88.73(6)	88.053
N4^{i}—Cu1—N5^{i}	91.27(6)	91.947
N5—Cu1—N5^{i}	180.00(8)	180
N4—Cu1—O5	93.31(7)	98.672
N4^{i}—Cu1—O5	86.69(7)	81.328
N5—Cu1—O5	90.64(7)	94.590
N5^{i}—Cu1—O5	89.36(7)	85.409

Cu(II) achieves an elongated octahedral coordination geometry through four nitrogen atoms of acetazolamide and nicotinamide ligands and two oxygen atoms of water molecules (Öztürk et al., 2012). DFT results showed that the bond lengths of nitrogen atoms in the axial position were elongated according to the XRD results (Cu1—N4; exp: 2.0147(16) Å calcd: 2.0365 Å and Cu1—N5; exp: 2.0490(16) Å calcd: 2.080 Å), while the bond lengths of the oxygen atoms in the apical position were shortened (Cu1—O5; exp: 2.5021 (19) Å calcd: 2.4568 Å) (Table 1).

The experimental and optimized structure with hydrogen atoms neglected was plotted overlapping as shown in Figure 1c. It was determined that the greatest change in bond lengths was observed around the S2 atom. The S2—O2, S2—O3 and S2—N4 bond lengths of Hacm in the complex were found as 1.4390(13) Å (calcd: 1.6291Å), 1.4443(15) Å (calcd:1.6532 Å) and 1.5430(16) Å (calcd:1.7289 Å), respectively. Compared with the calculated lengths of the free H_2acm (1.6375 Å, 1.6296 Å, and 1.8219 Å) (Das et al., 2015), the S2—O2, S2—O3 and S2—N4 bond lengths were elongated according to the complex. Since the calculations are in the gas phase, the hydrogen bond effect is not observed. This supports that this change in bond is caused by the hydrogen bond or the coordination.

The torsion angles on the R1—N—SO_2—R2 group of the acetazolamide anion in the complex were found to be 87.786º in the experimental structure and -147.202º in the optimized it. The RMSE value is found 0.288. This deviation value is due to the sulfa group of an acetazolamide anion.

Vibrational spectra

The FT-IR study of the Cu(II) complex was investigated observed and calculated values, the results are listed in Table 2. The calculations were executed DFT/B3LYP method and a 6-311G basis set. The calculated vibrational frequencies were scaled with 0.957, this value of the calculated H_2acm ligand was given as 0.92 in the literature (Öztürk et al., 2012).

Öztürk et al. (2012) found aqua OH groups participating in hydrogen bonding through the existence of υ(H_2O) bands at 3612 cm^{-1}. As a result of the theoretical calculations, the OH peak of the complex was calculated as 3774 cm^{-1}.

It is known that the acetazolamide ligand coordinates monodentately from the NH_2 group of the sulfonamide moiety to the Cu(II) ion. The ν(N-H) vibration bands in the IR spectrum of the complex showed an absorption band at 3139 cm^{-1}. Theoretically, it was calculated as 3609 cm^{-1}.

The band at about 3110 cm^{-1} corresponds to the N-H group of the amine form of the acetazolamide ligand, while the band at 2768 cm^{-1} is due to the N-H stretching vibration of the imine form. As a result of the theoretical calculation, the amine form was observed in 3447 cm^{-1} (Öztürk et al., 2012). While the asymmetric and symmetrical stretch modes of the CH_3 group were observed in the range of 3009-2844 cm^{-1}, they were calculated theoretically in the range of 3181-3060 cm^{-1}.

The asymmetric and symmetric stretching vibrations of the –SO_2 group in free H_2acm were observed at 1355s cm^{-1} and 1175 cm^{-1}. The symmetrical and asymmetrical stress vibrations of the –SO_2

group in the complex were observed at 1304 cm^{-1} and 1142 cm^{-1}. As a result of the theoretical calculation, it is seen that the correlation value is 0.918. It is expected that the SO_2 asymmetric and symmetric vibration values of the complex will be at higher frequencies.

When the experimentally obtained X-ray analysis results were examined, it was stated that the bond lengths of S2-O2 and S2-O3 of the complex were 1.4390 Å and 1.4443 Å (Öztürk et al., 2012). As a result of theoretical calculations, the bond lengths were obtained as 1.62914 Å, and 1.65316 Å, respectively.

The difference between the experimental and theoretical values in the asymmetric and symmetric vibration peaks of SO_2 is observed. Because the complex is an isolated molecule in which intermolecular interactions are ignored in the theoretical calculation of the complex, it is possible to understand the difference between the experimental and theoretical values of the asymmetric and symmetric SO_2 vibration peaks. This elongation observed in bond lengths can be explained by the fact that vibration frequencies shift to low frequencies (Al-Dawood, El -Metwaly, & El-Ghamry, 2016; Aycan, 2020; Öztürk, Bulut, Bekiroğlu, & Bulut, 2016).

Table 2: Observed and calculated vibrational frequencies of Cu(II) complex

Assig.	H_2acm	H_2acm (DFT)	na	Complex (exp) (Öztürk et al., 2012)	Complex (DFT)
$\nu(H_2O)$	-		-	3612m	3774
$\nu_{as}(NH_2)$	3300s	3601	-	-	-
$\nu_s(NH_2)$	3180s	3441	-	-	-
$\nu_{as}(NH_2)$	-	-	3368vs	3419 ws, 3375 sh, 3297vw	3764

$v_s(NH_2)$	-	-	3161s	3217 m	3614
v(N-H)$_{acm}$	-		-	3139 m	3609
v(N-H) $_{acm}$(RCONH)	3090w	3586	-	3110sh	3447
v(C-H)$_{na}$	-	-	3060sh	3070 w	3300, 3266, 3241, 3206
$v_{as}(CH_3)$	2990sh, 2935sh	3159, 3095	-	3009 w, 2934 w	3181, 3146
$v_{as}(H_2O)$					3031, 3022
$v_s(H_2O)$					
$v_s(CH_3)$	2900m	3033	-	2844 sh	3060
v(N-H)$_{ring}$ (imin tautomer)	2770m		-	2768 m	-
v(C=O)$_{na}$+ $\delta(NH_2)_{na}$	-		1697sh, 1679vs	1695 vs	1685
v(C=O)$_{acm}$	1680	1693	-	1681 s	1678
OH					1650
δ(N-H)$_{ip}$ NH_2 def	-	1602	1618vs	1622 m	1648, 1647
Ring str(py)	-	1549	1592vs	1601m	1638, 1637, 1607
v_{as}(C=N)$_{ring}$ (acm)	1540s		-	1539vs	1538, 1537
Ring str(py)	-		1484vs	1482w	
v_s(C=N)$_{ring}$ (acm)	1425 w		-	1439sh	
$\delta_{as}(CH_3)$	1415sh	1523	-	1422sh	1513
$\delta_s(CH_3)$	1370sh	1503	-	1376s	1492, 1440
$v_{as}(SO_2)$	1355s	871	-	1304vs	910, 908
v_{na}*(C-N-C)$_{ring}$*	1315s		-	-	1466
v_{acm}*(C-N)$_{ring}$*	1275m	1453	-	1279m	1441, 1431
v_{na}*(C-C)*	1240m			1243m	1390
Ring str(py)	-		1231w	1219w	1324, 1323
C-C str(py)	-		1204m	1205m	
$v_s(SO_2)$	1175s	736		1142vs	810, 808

NH_2 rock	-	1130	1154w	1155w	1257, 1253
v(C-N)$_{ring}$	1110m, 1040m, 1005m		-	1093w, 1034vw, 1014vw	1216, 1215
Ring breat(py)	-		1028ms	984s	1073, 1071, 1055
v(N-N)	975m		-	968vw	1054
v(SN)	910s		-	948w	810

Hirshfeld Surface Analysis

The Hirshfeld surfaces and 2D fingerprint calculations were performed using *Crystal Explorer 17.5* via cif files obtained as a result of single crystal X-ray diffraction (Clausen, Chevallier, Spackman, & Iversen, 2010; Spackman & Jayatilaka, 2009; Spackman & McKinnon, 2002). Hirshfeld surface analysis makes it easy to see the interaction trends of the crystal structure in packaging in a unique approach. With the Hirshfeld surface analysis, it is possible to separate the electron density of the crystal into molecular parts and to define the area where the molecule is located. Hirshfeld surface analysis helps to understand the role of non-covalent interactions such as hydrogen bonds and other intermolecular contacts (Clausen et al., 2010; McKinnon, Jayatilaka, & Spackman, 2007; McKinnon, Mitchell, & Spackman, 1998; Shit, Marschner, & Mitra, 2016; Spackman & Byrom, 1997; Spackman & Jayatilaka, 2009; Spackman, McKinnon, & Jayatilaka, 2008).

Two distances are defined for each point on the Hirshfeld surface: d_i and d_e express the distance of the nearest inner core and the nearest outer core to the Hirshfeld surface, respectively(Parkin et al., 2007; Spackman & McKinnon, 2002). The equation expressing the contact distance (d_{norm}) depending on the radius of d_i, d_e, and

vdW, as given in our previous study (Aycan, Öztürk, Demir, Özdemir, & Paşaoğlu, 2021), allows the identification of regions that are important for intermolecular interactions. A 2D fingerprint graph combined with d_e and d_i allows us to see the summary of intermolecular contacts in the crystal. In the Hirshfeld surface analysis, the d_{norm} can consist of red, white, and blue. If the intermolecular contacts are shorter than the van der Waals (vdW) radii, the dnorm value is negative, and if it is longer, it is positive. Interactions shown in red on Hirshfeld surfaces indicate areas of short contact, while interactions in blue indicate areas of long-range contact. The white areas represent contacts close to the van der Waals interaction (McKinnon, Spackman, & Mitchell, 2004; Sreenatha et al., 2020).

Hirshfeld surface analysis allows us to learn more about intermolecular interactions as well as visualize intermolecular interactions. Examining the intermolecular interactions between the target molecule and the corresponding receptor is very important in terms of understanding the biological activities of the developed complexes.

The intermolecular interactions of the complex are investigated using Hirshfeld surface analysis. The mapping of d_i, d_e, d_{norm} (-0.5561 to 1.2590), shape index (-1 to 1), and curvedness (-4 to 0.4) are as shown in Figure 3

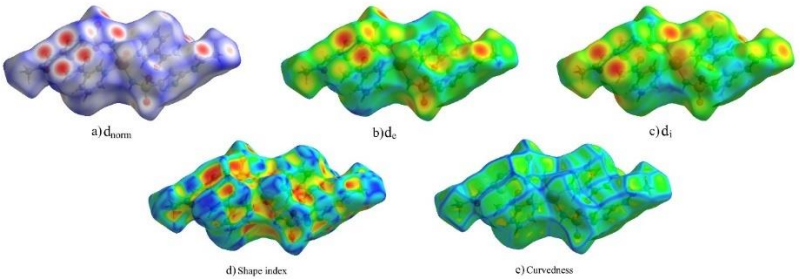

Figure 3: Hirshfeld surfaces mapped with d_{norm} (upper left), d_e (upper middle), d_i (upper right), shape index (bottom left), and curvedness (bottom right) of the complex.

The 2D fingerprint representation of O·· H, N·· H, and H···H which have the greatest contributions to intermolecular interactions as a result of Hirshfeld surface analysis is given in Figure 4**.** These values are C·· H/H·· C (6.7%), O·· H/H·· O (42.9%), N·· H/H·· N (13.4%), S···H/H·· S (4.4%) and H···H/H·· H (21.7%) (Table 3).

Table 3: Percentage contribution to interatomic contacts from the Hirshfeld surface for complex

Contact	Contribution (%)
N···H/H···N	8.5
O···H/ H···O	30.6
C···H/H···C	15.5
H···H	43.4
C···O/O···C	0.2
N···O/O···N	0.8
O···O	1.0
All···O	15.9
All···N	4.2
All···H	73.0
All···C	6.9
N···All	5.2
O···All	17.5
H···All	68.4
C···All	8.8
All···All	100.0

As seen in Figure 5, the red spots expressing the donor-acceptor interaction result from intermolecular interactions of N6—H6···N2^{ii}, N3—H1···O4^{ii}, N6—H7···O3^{iii} and C7—H9···O3 (Table 4). In Table 4, short intermolecular interactions of the complex according to the XRD and Hirshfeld results are given.

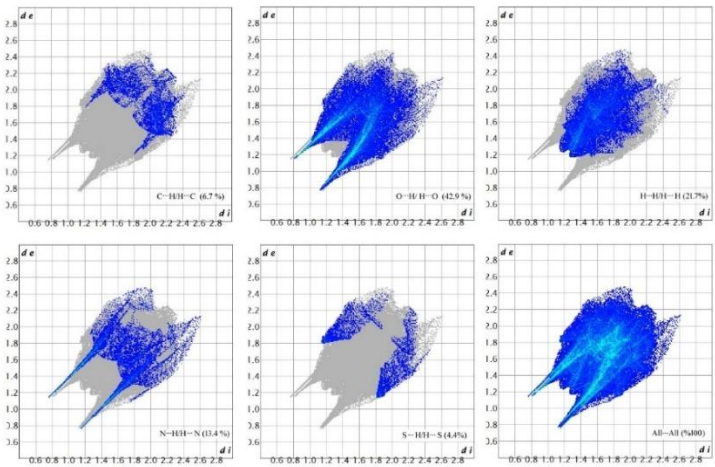

Figure 4: (a) C···H, (b) O···H, (c) H···H, (d) N···H and (e) S···H contacts showing the percentages of contacts contributed to the total Hirshfeld surface area.

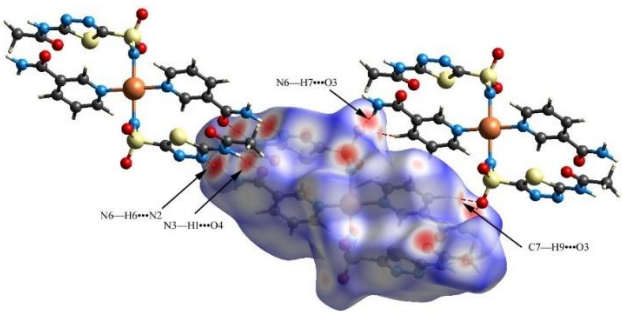

Figure 5. Fingerprint of the Cu(II) complex having scattering points of contacts

Table 5: Short intermolecular interactions in the complex based on XRD and Hirshfeld results

Interactions	H···A (XRD) Å	H···A (Hirshfeld) Å
N6—H6···N2^{ii}	2.911	2.411
N3—H1···O4^{ii}	2.973	2.972
N6—H7···O3^{iii}	3,074	3.074
C7—H9···O3	3.427	3.200

Chemical reactivity

Quantum chemical data of the complex and free ligand are comparatively given in Table 5. E_{gap} values are found for Cu(II) complex 4.35 eV (α), 3.73 eV (β), and for acetazolamide 3.58 eV. According to Table 5, the ligand has a greater hardness, the complex has greater softness. So, the complex has higher chemical activity and lower kinetic stability. The electronegativity of the complex is lower than H_2acm. Therefore, the electron received ability of the complex is lower and more stable. When the biological activities of the Cu(II) complex and H_2acm ligand were compared, it was determined that the biological activity of the complex was higher than that of H_2acm. Because the complex form of H_2acm has a higher electrophilic index, ΔN_{MAX}, S, and lower nucleophilic index.

Table 5: Quantum chemical descriptors of complex

	Cu(II) complex DFT-B3LYP/LanL2DZ		Acetazolamide DFT-B3LYP/6311-G
	α	β	
E_{HOMO}(eV)	-6.40	-6.58	-7.91
E_{LUMO}(eV)	-2.05	-2.85	-2.56
E_{GAP}(eV) ($\lvert E_{HOMO} - E_{LUMO} \rvert$) Energy band gap	4.35	3.73	5.35
I(eV)	6.40	6.58	6.34

$(-E_{HOMO})$ Ionization potential			
A(eV) $(-E_{LUMO})$ Electron affinity	2.05	2.85	1.76
η(eV) $\left(\frac{(I-A)}{2}\right)$ Chemical hardness	2.18	1.87	2.68
σ(eV^{-1}) $\left(\frac{1}{\eta}\right)$ Chemical softness	0.46	0.53	0.37
χ(eV) $\left(\frac{(I+A)}{2}\right)$ Electronegativity	4.23	4.23	4.05
μ(eV) $-\left(\frac{(I+A)}{2}\right)$ Chemical potential	-4.23	-4.23	-4.05
ω(eV) $\left(\frac{\mu^2}{2\eta}\right)$ Electrophilic index	4.10	4.78	3.06
N(eV^{-1}) $\left(\frac{1}{\omega}\right)$ Nucleophilic index	0.24	0.21	0.33
ΔN_{MAX} $\left(-\frac{\mu}{\eta}\right)$ Maximum charge transfer	1.94	2.26	1.51
S(eV^{-1}) $\left(\frac{1}{2\eta}\right)$ Global Softness	0.23	0.27	0.19

Molecular Docking Studies

In pharmaceutical and medicine, molecular docking works are an important calculation technique to estimate the interactions in

ideal protein, DNA, or RNA binding sites in the cavity. Sulfonamides are analogs of PABA (antimetabolite) and enter folic acid synthesis by competing with it for the enzyme dihydropteroate synthetase (DHPS). They inhibit folic acid synthesis. As a result, RNA and DNA synthesis is impaired in bacteria(Hussein, 2018; Sahua et al., 2017). Therefore, sulfonamide connected crystal structure of DHPS of Yersinia pestis has been downloaded from PDB (PBD ID: 3TZF, https://www.rcsb.org/structure/3TZF) (Yun et al., 2012). The optimized structure with minimum energy of the complex has been calculated by the DFT method. The docking study has been performed to predict the most probable mode of binding of the complex with dihydropteroate synthase (DHPS) by Autodock 4.2.6 and Autodock Tool 1.5.6 (Sanner, 1999; Trott & Olson, 2010) and BIOVIA Discovery Studio Visualizer software 2019 (D. S. V. Biovia). GLY225, ASN229, PHE28, GLN149, SER222, GLN226, ARG235, PRO232, ARG63, and PRO64 are the active sites, that are ten amino acid residues (Table 6). The seven amino acids (GLY225, ASN229, PHE28, GLN149, SER222, GLN226, ARG235) of the complex form nine hydrogen bonds in total (Figure 6). Protein-ligand binding energy of the complex is found -8.3 kcal.mol^{-1}.

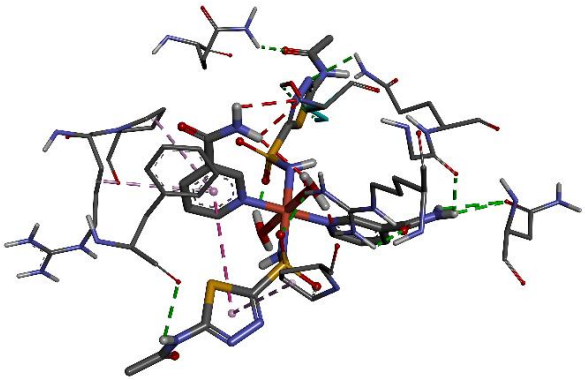

(a)

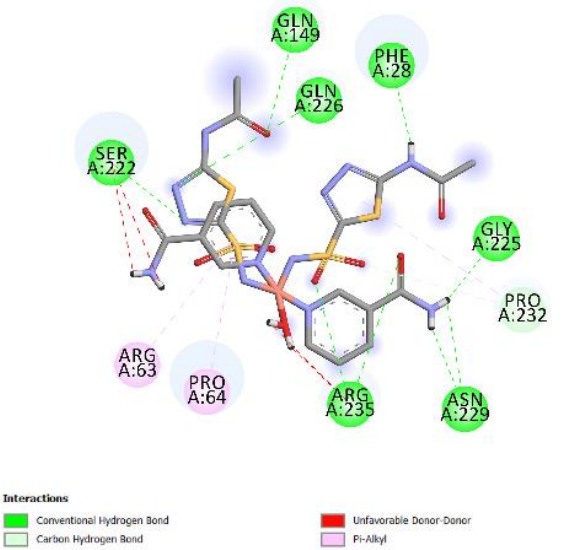

(b)

Figure 6: (a) 3D (b) 2D docking image of the copper complex with DHPS of Yersinia pestis (PDB ID:3TZF)

Table 6: Details of interactions in most stable for complex–protein interaction

Distance (Å)	Binding Type	Receptor binding site	Compound binding site	Binding Mode
2.3714	H-Bond	A:GLY225:O	Complex: H	H-D→ H-A
2.70229	H-Bond	A:ASN229:OD1	Complex: H	H-D→ H-A
2.98728	H-Bond	A:ASN229:OD1	Complex: H	H-D→ H-A
2.95762	H-Bond	A:PHE28:O	Complex: H	H-D→ H-A
2.47975	H-Bond	A:GLN149:HE22	Complex: O	H-D→ H-A
2.55622	H-Bond	A:SER222:HG	Complex: N	H-D→ H-A
2.11416	H-Bond	A:SER222:HG:B	Complex: N	H-D→ H-A
2.80606	H-Bond	A:GLN226:HE21	Complex: N	H-D→ H-A
2.27964	H-Bond	A:ARG235:HH12	Complex: O	H-D→ H-A
2.54091	H-Bond	A:ARG235:HH21	Complex: O	H-D→ H-A
3.6109	Carbon H-Bond	A:PRO232:CD	Complex: O	H-D→ H-A
4.98182	π - Alkyl	A:ARG63	Complex	π-orbital→ Alkyl
4.95645	π - Alkyl	A:PRO64	Complex	π-orbital→ Alkyl
4.74128	π - Alkyl	A:PRO232	Complex	π-orbital→ Alkyl

H-D: H-Donor; H-A:H-Acceptor

Druglikeness and ADMET studies

The physicochemical data of the complex and the reference drug (acetazolamide) were calculated using OpenBabel Gui software and SwissADME (Norinder & Bergström, 2006). We can distinguish druglikeness properties according to Lipinski's five rules given below (Lipiński, 2001).

- MW< 500 g/mol,
- MLogP<4.15,
- H-A (number of H-bond acceptors) < 5,
- H-D (number of H-bond donors) < 10,
- 40< MR (Molar refraction) <130.

It can be said that molecules that comply with 2 or more of these rules have high drug-like properties. Investigation of these properties can help in early preclinical developments and prevent costly late pre-clinical and clinical failures. To find out the drug-like properties, H_2acm was evaluated using Lipinski's rule of five, except complex. The results are given in Table 7. Results showed that H_2acm (acetazolamide) owned the drug-likeness properties, more than or like complex. The solubility and lipophilicity properties of the complex were presented in the form of Log S and WLog P, respectively. According to the results, it was found that the complex has lower gastrointestinal permeability than H_2acm. TPSA values of acetazolamide predicted approximately three times better cell internalization to the complex. The synthesized complex is found to be all Lipinski violations. Hence, it implies that this complex does not have the drug ability properties/druglikeness properties. So, it

may be concluded that H_2acm may have drug likeness properties than the complex.

Table 7: The physicochemical properties and druglikeness of the compounds

Compound	Complex	H_2acm
Molecular Weight (g/mol)	788.32	222.25
no. of H-bond acceptors	16	6
no. of H-bond donor	8	2
LogS (Solubility)	-2.21	-1.14
TPSA (Total polar surface area)	386.46	151.66
Rotatable bonds	14	3
MR (Molar refractivity)	167.71	45.22
Number of atoms	47	13
Lipinski violations	5	0
WLogP (Lipophilicity)	-6.68	2.26
Synthetic Accessibility	5.25	2.73
Gastrointestinal	Low	Low
BBB (Blood-brain barrier)	No	No
P-gp (P-glycoprotein)	Yes	No
CYP1A2 inhibitor	No	No
CYP2C6 inhibitor	No	No
$LogK_p$ (Skin permeation (cm/s))	-13.08	-7.84

CYP2D6= cytochrome P450 family 2 subfamily D member 6 (PDB:5TFT); CYP1A2= cytochrome P450 family 1 subfamily A member 2 (PDB: 2HI4)

Conclusion

All theoretical calculations of the $[Cu(Hacm)_2(na)_2(H_2O)_2]$ complex were performed with DFT/B3LYP/LANL2DZ. The investigated complex was found to be quite compatible with the theoretical geometric data compared to a complex. While the optimized complex was in the energy range ΔE=-4.35 (alpha) -3.73

(beta) eV, the energy range of the free H_2acm ligand was found to be -5.35 eV. It was observed that the complex exhibited better chemical and biological activity than the free ligand. With the Hirshfeld surface analysis method, intermolecular interactions, the % contribution of the interactions of atoms with each other, fingerprint determination, and the display of the total surface maps were made. In the molecular chelation analysis, the best chelation modulus and binding energy of the complex and DHPS of Yersinia pestis protein were found to be -8.3 kcal/mol. Most of the interactions between the complex and the protein are conventional hydrogen bonding. The result of molecular chelation analysis was found to be quite high, although there are difficulties in drug production, the biological activity of the metal complex is higher than the free acetazolamide ligand. According to ADME results, it can be said that the drug production of the complex is quite difficult.

Referance

Akocak, S., Lolak, N., Nocentini, A., Karakoc, G., Tufan, A., & Supuran, C. T. (2017). Synthesis and biological evaluation of novel aromatic and heterocyclic bis-sulfonamide Schiff bases as carbonic anhydrase I, II, VII and IX inhibitors. *Bioorganic & Medicinal Chemistry, 25*(12), 3093-3097. doi:https://doi.org/10.1016/j.bmc.2017.03.063

Al-Dawood, A. Y., El -Metwaly, N. M., & El-Ghamry, H. A. (2016). Molecular docking and DFT studies on some nano-meter binuclear complexes derived from hydrazine-carbothioamide ligand, synthesis, thermal, kinetic and spectral characterization. *Journal of Molecular Liquids, 220*, 311-323. doi:https://doi.org/10.1016/j.molliq.2016.04.079

Aycan, T. (2020). Hekzaakua-bis(sulfat) içeren nikotinamitli kobalt(II) ve çinko(II) koordinasyon bileşikleri: sentezlenmesi, yapısal, spektroskopik ve termal özelliklerinin incelenmesi. In C. C. Ersanlı, E. Tezel Ersanlı, & C. Başlak (Eds.), *Geleceğin Dünyasında Bilimsel ve Mesleki Çalışmalar 2020/ Fen Bilimleri I* (pp. 94-111). Bursa: Ekin Basım Yayın Dağıtım.

Aycan, T., Öztürk, F., Demir, S., Özdemir, N., & Paşaoğlu, H. (2021). Cobalt(III) complex of substituted nalidixic acid: Synthesis, characterization (IR, UV, EPR), single crystal X-ray, antimicrobial activity, Hirshfeld surface analysis and molecular docking. *Journal of Molecular Structure, 1225*, 129043. doi:https://doi.org/10.1016/j.molstruc.2020.129043

Banerjee, P., Dehnbostel, F. O., & Preissner, R. (2018). Prediction Is a Balancing Act: Importance of Sampling Methods to

Balance Sensitivity and Specificity of Predictive Models Based on Imbalanced Chemical Data Sets. *Frontiers in Chemistry, 6*. doi:https://doi.org/10.3389/fchem.2018.00362

Banerjee, P., Eckert, A. O., Schrey, A. K., & Preissner, R. (2018). ProTox-II: a webserver for the prediction of toxicity of chemicals. *Nucleic acids research, 46*(W1), W257-W263. doi:https://doi.org/10.1093/nar/gky318

Becke, A. D. (1993). Density-functional thermochemistry. III. The role of exact exchange. *The Journal of Chemical Physics, 98*(7), 5648-5652. doi:10.1063/1.464913

Bertini, I., Gray, H. B., Lippard, S. J., & Valentine, J. S. (1994). *Bioinorganic chemistry*: University science books.

BIOVIA, D. S. BIOVIA Discovery Studio Visualizer, v16. 1.0. 15350, San Diego: Dassault Systemes; 2015 [cited: 2017 Mar 20]. In.

Biovia, D. S. V. Version 19.1. 0.18287 Software; 2019. *Avaliable from: http://www. 3dsbiovia. com/.[Last accessed on 2019 Jul 20]*.

Check, C. E., Faust, T. O., Bailey, J. M., Wright, B. J., Gilbert, T. M., & Sunderlin, L. S. (2001). Addition of Polarization and Diffuse Functions to the LANL2DZ Basis Set for P-Block Elements. *The Journal of Physical Chemistry A, 105*(34), 8111-8116. doi:10.1021/jp011945l

Chiodo, S., Russo, N., & Sicilia, E. (2006). LANL2DZ basis sets recontracted in the framework of density functional theory. *The*

Journal of Chemical Physics, 125(10), 104107. doi:10.1063/1.2345197

Clausen, H. F., Chevallier, M. S., Spackman, M. A., & Iversen, B. B. (2010). Three new co-crystals of hydroquinone: crystal structures and Hirshfeld surface analysis of intermolecular interactions. *New Journal of Chemistry, 34*(2), 193-199.

Daina, A., Michielin, O., & Zoete, V. (2017). SwissADME: a free web tool to evaluate pharmacokinetics, drug-likeness and medicinal chemistry friendliness of small molecules. *Scientific Reports, 7*(1), 42717. doi:https://doi.org/10.1038/srep42717

Das, D., Sahu, N., Roy, S., Dutta, P., Mondal, S., Torres, E. L., & Sinha, C. (2015). The crystal structure of sulfamethoxazole, interaction with DNA, DFT calculation, and molecular docking studies. *Spectrochimica Acta Part A: Molecular and Biomolecular Spectroscopy, 137,* 560-568.

Dennington II, R., Keith, T., & Millam, J. (2009). GaussView 5.0, Wallingford, CT.

Diaz, J. R. A., Camí, G. E., Liu-González, M., Vega, D. R., Vullo, D., Juárez, A., . . . Supuran, C. T. (2016). Salts of 5-amino-2-sulfonamide-1,3,4-thiadiazole, a structural and analog of acetazolamide, show interesting carbonic anhydrase inhibitory properties, diuretic, and anticonvulsant action. *Journal of Enzyme Inhibition and Medicinal Chemistry, 31*(6), 1102-1110. doi:10.3109/14756366.2015.1096270

Drwal, M. N., Banerjee, P., Dunkel, M., Wettig, M. R., & Preissner, R. (2014). ProTox: a web server for the in silico prediction

of rodent oral toxicity. *Nucleic acids research, 42*(W1), W53-W58. doi:https://doi.org/10.1093/nar/gku401

Frisch, M., Trucks, G. W., Schlegel, H. B., Scuseria, G. E., Robb, M. A., Cheeseman, J. R., . . . Petersson, G. e. (2014). Gaussian~ 09 Revision D. 01.

Frisch, M. J., Pople, J. A., & Binkley, J. S. (1984). Self-consistent molecular orbital methods 25. Supplementary functions for Gaussian basis sets. *The Journal of Chemical Physics, 80*(7), 3265-3269. doi:10.1063/1.447079

Health, N. I. o. (2002). Journal of enzyme inhibition and medicinal chemistry.

Hussein, M. F. (2018). New sulfonamide hybrids: synthesis, in vitro antimicrobial activity and docking study of some novel sulfonamide derivatives bearing carbamate/acyl-thiourea scaffolds. *Mediterranean Journal of Chemistry, 7*(5), 370-385.

Lee, C., Yang, W., & Parr, R. G. (1988). Development of the Colle-Salvetti correlation-energy formula into a functional of the electron density. *Physical Review B, 37*(2), 785-789. doi:10.1103/PhysRevB.37.785

Lipiński, E. (2001). *Semitic languages: outline of a comparative grammar* (Vol. 80): Peeters Publishers.

McKinnon, J. J., Jayatilaka, D., & Spackman, M. A. (2007). Towards quantitative analysis of intermolecular interactions with Hirshfeld surfaces. *Chemical Communications*(37), 3814-3816.

McKinnon, J. J., Mitchell, A. S., & Spackman, M. A. (1998). Hirshfeld surfaces: a new tool for visualising and exploring

molecular crystals. *Chemistry–A European Journal*, *4*(11), 2136-2141.

McKinnon, J. J., Spackman, M. A., & Mitchell, A. S. (2004). Novel tools for visualizing and exploring intermolecular interactions in molecular crystals. *Acta Crystallographica Section B: Structural Science*, *60*(6), 627-668.

Norinder, U., & Bergström, C. A. (2006). Prediction of ADMET properties. *ChemMedChem: Chemistry Enabling Drug Discovery*, *1*(9), 920-937. doi: https://doi.org/10.1002/cmdc.200600155

O'boyle, N. M., Tenderholt, A. L., & Langner, K. M. (2008). Cclib: a library for package-independent computational chemistry algorithms. *Journal of computational chemistry*, *29*(5), 839-845.

Öztürk, F., Bulut, A., Paşaoğlu, H., Bulut, İ., & Büyükgüngör, O. (2012). Structural, spectroscopic and voltammetric studies of bis(acetazolamido)bis(aquo)bis(nicotinamide)copper(II). *Spectrochimica Acta Part A: Molecular and Biomolecular Spectroscopy*, *97*, 24-30. doi:https://doi.org/10.1016/j.saa.2012.05.036

Öztürk, F., Bulut, İ., Bekiroğlu, Y., & Bulut, A. (2016). Spectroscopic, structural, electrochemical and antimicrobiological studies of Cu(II)-sulfathiazole complex with diethylenetriamine ligand. *Polyhedron*, *119*, 420-428. doi:https://doi.org/10.1016/j.poly.2016.07.019

Parkin, A., Barr, G., Dong, W., Gilmore, C. J., Jayatilaka, D., McKinnon, J. J., . . . Wilson, C. C. (2007). Comparing entire crystal structures: structural genetic fingerprinting. *CrystEngComm, 9*(8), 648-652.

Saczewski, F., Innocenti, A., Brzozowski, Z., Sławiński, J., Pomarnacka, E., Kornicka, A., . . . Supuran, C. T. (2006). Carbonic anhydrase inhibitors. Selective inhibition of human tumor-associated isozymes IX and XII and cytosolic isozymes I and II with some substituted-2-mercapto-benzenesulfonamides. *Journal of Enzyme Inhibition and Medicinal Chemistry, 21*(5), 563-568. doi:10.1080/14756360600648146

Sahua, N., Mondala, S., Naskara, K., Guptab, S., Kaleeswaranc, D., & Sinha, C. (2017). Structure, antimicrobial activity and molecular docking study of novel o-vaniline based sulfamethoxazolyl derivatives. *J. Indian Chem. Soc, 94*, 1387-1401.

Sanner, M. F. (1999). Python: a programming language for software integration and development. *J Mol Graph Model, 17*(1), 57-61.

Scozzafava, A., & Supuran, C. T. (2014). Glaucoma and the applications of carbonic anhydrase inhibitors. *Carbonic Anhydrase: Mechanism, Regulation, Links to Disease, and Industrial Applications*, 349-359.

Shit, S., Marschner, C., & Mitra, S. (2016). Synthesis, crystal structure, and Hirshfeld surface analysis of a new mixed ligand copper (II) complex. *Acta Chimica Slovenica, 63*(1), 129-137.

Singh, P., Swain, B., Thacker, P. S., Sigalapalli, D. K., Purnachander Yadav, P., Angeli, A., . . . Arifuddin, M. (2020). Synthesis and carbonic anhydrase inhibition studies of sulfonamide based indole-1,2,3-triazole chalcone hybrids. *Bioorganic Chemistry, 99*, 103839. doi:https://doi.org/10.1016/j.bioorg.2020.103839

Spackman, M. A., & Byrom, P. G. (1997). A novel definition of a molecule in a crystal. *Chemical physics letters, 267*(3-4), 215-220.

Spackman, M. A., & Jayatilaka, D. (2009). Hirshfeld surface analysis. *CrystEngComm, 11*(1), 19-32.

Spackman, M. A., & McKinnon, J. J. (2002). Fingerprinting intermolecular interactions in molecular crystals. *CrystEngComm, 4*(66), 378-392.

Spackman, M. A., McKinnon, J. J., & Jayatilaka, D. (2008). Electrostatic potentials mapped on Hirshfeld surfaces provide direct insight into intermolecular interactions in crystals. *CrystEngComm, 10*(4), 377-388.

Sreenatha, N., Chakravarthy, A. J., Suchithra, B., Lakshminarayana, B., Hariprasad, S., & Ganesha, D. (2020). Crystal, spectral characterization, molecular docking, Hirshfeld computational studies and 3D-energy framework analysis of a novel puckered compound (C14H15Cl O): 2-Chloro-3-phenyl-5, 5-dimethylcyclohex-2-en-1-one. *Journal of Molecular Structure, 1210*, 127979.

Supuran, C. T. (2012). Structure-based drug discovery of carbonic anhydrase inhibitors. *Journal of Enzyme Inhibition and Medicinal Chemistry, 27*(6), 759-772.

Supuran, C. T., Casini, A., & Scozzafava, A. (2004). Development of sulfonamide carbonic anhydrase inhibitors. In *Carbonic Anhydrase* (pp. 79-160): CRC Press.

Trott, O., & Olson, A. J. (2010). AutoDock Vina: improving the speed and accuracy of docking with a new scoring function, efficient optimization, and multithreading. *Journal of computational chemistry, 31*(2), 455-461. doi: https://doi.org/10.1002/jcc.21334

Turner, M., McKinnon, J., Wolff, S., Grimwood, D., Spackman, P., Jayatilaka, D., & Spackman, M. (2017). CrystalExplorer17: The University of Western Australia Perth, WA, Australia.

Yun, M.-K., Wu, Y., Li, Z., Zhao, Y., Waddell, M. B., Ferreira, A. M., . . . White, S. W. (2012). Catalysis and sulfa drug resistance in dihydropteroate synthase. *Science, 335*(6072), 1110-1114.

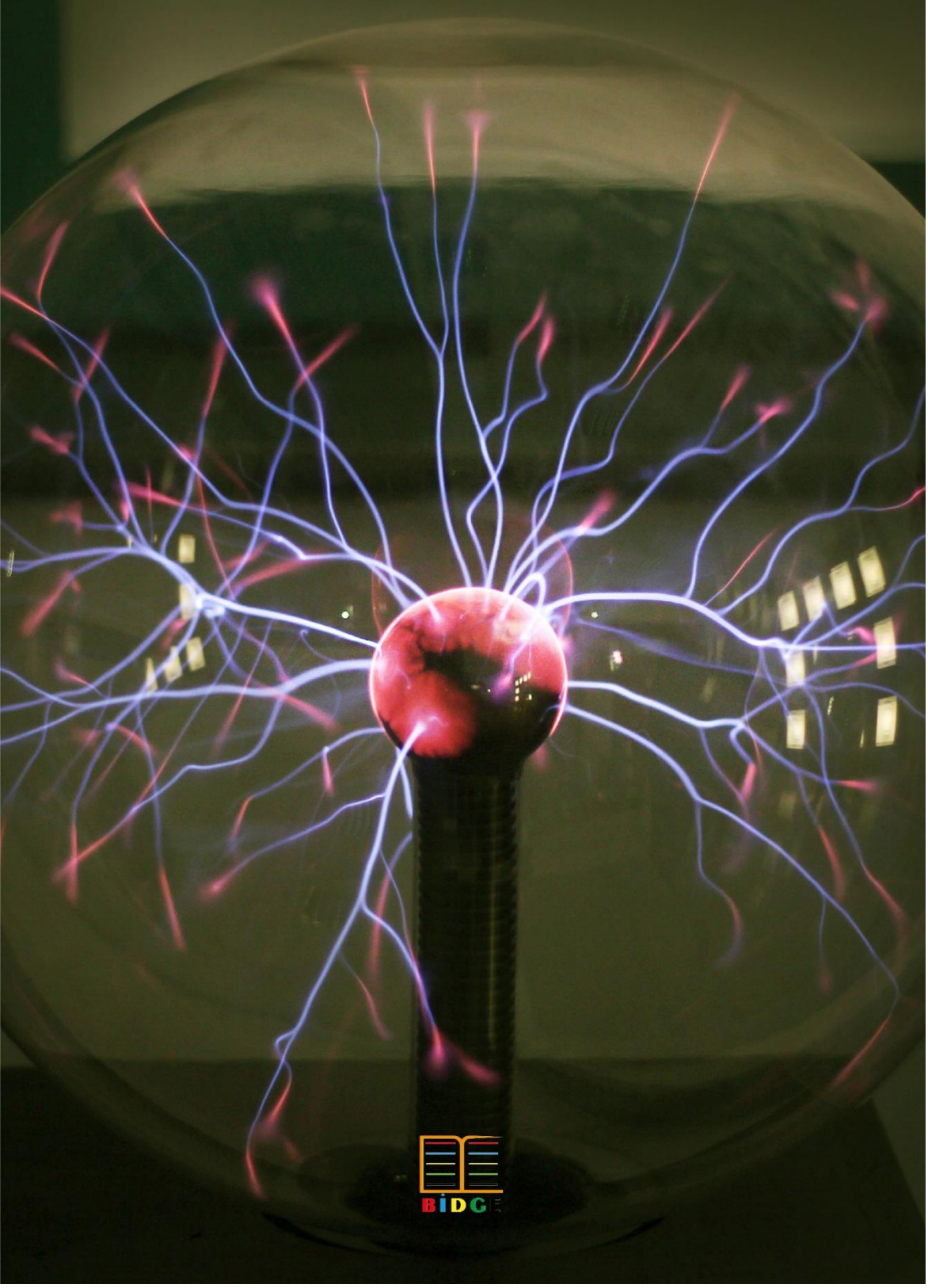
BİDGE